Precision Control of High Speed Drives using Active Vibration Damping

by

Daniel Gordon

A thesis
presented to the University of Waterloo
in fulfillment of the
thesis requirement for the degree of
Master of Applied Science
in
Mechanical Engineering

Waterloo, Ontario, Canada, 2010

AUTHOR'S DECLARATION

I hereby declare that I am the sole author of this thesis. This is a true copy of the thesis, including any required final revisions, as accepted by my examiners.

I understand that my thesis may be made electronically available to the public.

Abstract

In order to meet industry demands for improved productivity and part quality, machine tools must be equipped with faster and more accurate feed drives. Over the past two decades, research has focused on the development of new control strategies and smooth trajectory generation techniques. These developments, along with advances in actuator and sensor technology, have greatly improved the accuracy of motion delivery in high speed machine tools. However, further advancement is limited by the vibration of the machine's structure. The purpose of the research in this thesis is to develop new control techniques that use active vibration damping to achieve bandwidths near the structural frequencies of machine tools, in order to provide better dynamic positioning of the tool and workpiece.

Two machine tool drives have been considered in this study. The first is a precision ball screw drive, for which a pole-placement technique is developed to achieve active vibration damping, as well as high bandwidth disturbance rejection and positioning. The pole-placement approach is simple and effective, with an intuitive physical interpretation, which makes the tuning process straightforward in comparison to existing controllers which actively compensate for structural vibrations. The tracking performance of the drive is improved through feedforward control using inverted plant dynamics and a novel trajectory pre-filter. The pre-filter is designed to remove tracking error artifacts correlated to the velocity, acceleration, jerk and snap (4th derivative) of the commanded trajectory. By applying the least-squares method to the results of a single tracking experiment, the pre-filter can be tuned quickly and reliably. The proposed controller has been compared to a controller used commonly in industry (P-PI position-velocity cascade control), and has achieved a 40-55 percent reduction in peak errors during tracking and machining tests. The controller design, stability analysis, and experimental results are discussed.

The second drive considered is a linear motor driven X-Y stage arranged as a T-type gantry and worktable. The worktable motion is controlled independently of the gantry using a loop shaping filter. The gantry is actuated by dual direct drive linear motors and is strongly coupled to the worktable position, which determines its inertial characteristics. A 94 Hz yaw mode is handled in the gantry control law using sensor and actuator averaging, and active vibration damping. The stability and robustness of the design are considered using multivariable frequency domain techniques. For the worktable motion along the gantry, a bandwidth of 130 Hz is achieved. The gantry crossover frequency is 52 Hz, which is 3 times higher than the bandwidth that can be achieved using independent PID controllers (16 Hz). The

performance of the proposed control scheme has been verified in step disturbance (i.e., rope snap) tests, as well as tracking and contouring experiments.

Acknowledgements

Dedication

To Monica and my parents

Table of Contents

List of Figures

List of Tables

Chapter 1

Introduction

The manufacturing industry is continually pushing for reductions in cycle times and more stringent tolerances, in order to maximize productivity and produce higher quality products. As a result, the demands on machine tools continue to rise. In order to take advantage of improvements in other areas of machine tool engineering, such as increasing spindle speeds and the introduction of more advanced tooling, feed drives must be able to deliver higher speeds while maintaining or improving positioning accuracy. Over the past two decades, research into new control strategies and smooth trajectory generation, along with improvements in actuator and sensor technology, have greatly enhanced the motion delivery provided by high speed feed drives.

In order to realize the most favorable command tracking and disturbance rejection properties in feed drives, a high closed-loop bandwidth must be obtained [29]. Structural vibrations of the drive and machine tool can severely limit the control bandwidth. Some of the methods that have been proposed in literature to deal with such vibrations include pre-filtering of the motion commands [17] and notch filtering of the control signal to attenuate actuation near the resonances [33]. More recently, controllers that use ball screw drives or linear motors to actively compensate for structural dynamics have been developed, as reported in [2][19][31][34]. This approach enables higher bandwidths to be achieved, but the design becomes more difficult as higher order plant models must be considered.

In ball screw drives, the first axial mode is the limiting factor in achieving high control bandwidths. In this thesis, a new method of providing active vibration damping for ball screw drives using pole-placement control is introduced. This method uses a physically meaningful model and provides an intuitive choice of closed-loop pole locations.

On the other hand, machines which utilize direct drive linear motors are increasing in popularity. Direct drives have many advantages over conventional ball screw drives in terms of dynamic response and accuracy. However, they are also more susceptible to disturbance forces and inertia variations, due to the lack of gear ratio between the motor and load. Some of these direct drive machines are arranged in gantry configurations, which result in one axis being actuated by parallel drives. These drives will inevitably be coupled through the gantry inertia and vibrations. As a result, achieving a high control bandwidth and ensuring stability is a significant challenge.

In this thesis, a dynamic model for a T-type gantry has been developed, which captures the dynamics of the first vibration mode. Using insight from this model, a multi-input, multi-output (MIMO) control law consisting of a sensor/actuator averaging scheme with active vibration damping has been designed.

The subsequent chapters in this thesis are arranged as follows:

A literature review on existing modeling, identification and control techniques for machine tool feed drives is presented in Chapter 2. In particular, modeling and control of higher order dynamics is relevant to the goal of this thesis. Modeling of rigid-body dynamics and nonlinear friction, as well as feedforward controller design have also been discussed.

In Chapter 3, pole-placement control is used to actively dampen the 1st mode of axial vibrations in a ball screw drive. Trajectory tracking is improved through feedforward control, using inverted plant dynamics, feedforward friction compensation, and a Least Squares tuned trajectory pre-filter. Effectiveness of the proposed strategy is verified in frequency domain analyses and also in rope-snap testing, trajectory tracking and metal cutting experiments. The proposed scheme is compared to the mainstream P-PI cascade design used in industry.

The sensor and actuator averaging concept has been adopted in a novel controller design for a T-type gantry in Chapter 4. The control law has been designed to take into account the dynamic coupling between the actuators and to actively attenuate the first vibration mode encountered at 94 Hz on the gantry. The stability and robustness of the design is achieved through the use of multivariable frequency domain analyses.

Chapter 2
Literature Review

This chapter is dedicated to reviewing some of the work done by other researchers which is relevant to the topics addressed in this thesis. Section 2.1 reviews past research into the modeling and identification of ball screw drives and direct-driven machine tools. Different approaches to the feedback controller design of these machines have been presented in Section 2.2. Finally, Section 2.3 covers feedforward control concepts.

2.1 Modeling and Identification

Much research has been devoted to the modeling of ball screw drives and direct-driven machine tools, including the modeling of their structural flexibility. Dynamic modeling can be performed at many different levels of detail and complexity, ranging from rigid body models to complicated models built using finite element methods (FEM). In this section, modeling of the rigid body dynamics, structural vibrations, and nonlinear friction are discussed.

2.1.1 Rigid Body Dynamics

Rigid body modeling attempts to capture the low frequency behavior of the system, basically consisting of the effects of inertia, viscous damping and Coulomb friction effects.

Direct drives are generally not prone to the low-frequency modes that plague ball screw drives. This allows them to generally be modeled as a pure mass with viscous damping [37]. This is one of the approaches employed in Chapter 4. However, when direct drives are arranged in gantry configurations, crosstalk through the inertia and low-frequency structural vibrations of the gantry is inevitable. In literature, Teo et al. [35] have developed a rigid body dynamic model for an H-type gantry, neglecting vibration modes and stiffness values.

2.1.2 Structural Vibrations

Structural vibrations in machine tools can severely limit the controller performance. In particular, if no method of avoiding excitation or damping of the vibrations is implemented, the achievable closed-loop bandwidth will be significantly below the frequency of the 1st vibration mode [28]. In order to apply

vibration compensation, knowledge of the vibration mode is essential. In literature, approaches to modeling the structural vibrations include analytical methods [6][38], frequency response measurement [8][33][38] and finite element methods [1][8][26][33][42].

A lumped model can be used to represent the vibratory dynamics, such as the one developed analytically by Varanasi and Nayfeh [38] for the 1st axial mode of a ball screw. A similar approach using a 2-DOF model with a diagonal mass matrix was used by Kamalzadeh and Erkorkmaz [19] to model the 1st axial mode of a ball screw. This model is used in Chapter 3 of this thesis. A 2-DOF model with a full mass matrix and least-squares identification using experimental frequency response data similar to the method used by Okwudire in [27] is used in Chapter 4.

2.1.3 Friction

Friction is a significant source of disturbance in machine tools. In particular, friction causes errors during motion reversals, since the controller integral action cannot immediately respond to the discontinuous change in the friction force as the velocity crosses through zero. Accurate identification and feedforward compensation can help to reduce these positioning errors.

Friction modeling and compensation techniques that include the Stribeck effect [4] have been presented in literature [4][9][21]. The nonlinear friction disturbance, in simplified form, can be modeled as,

$$d(v) = \begin{cases} d_c^+ + (d_s^+ - d_c^+)e^{-|v|/\Omega} & \text{when } v > 0 \\ 0 & \text{when } v = 0 \\ d_c^- + (d_s^- - d_c^-)e^{-|v|/\Omega} & \text{when } v < 0 \end{cases} \qquad (2.1)$$

where d_c is the Coulomb friction, d_s is the static friction, v is the velocity and Ω is the velocity constant. A method of identifying the model parameters using Kalman filtering [18] to estimate the equivalent disturbance has been used in this work following the method in [9]. Feedforward friction compensation using the identified model is implemented in Chapter 3.

2.2 Control Law Design and Active Vibration Damping

The main objectives of feedback control are to reject disturbances and accurately follow commands. In [29], the importance of a high closed-loop bandwidth for command tracking and disturbance rejection was noted. Designing a controller based on rigid-body dynamics and neglecting structural resonances significantly limits the achievable bandwidth [28].

4

Notch filters in the control loop can also be used to mitigate the effect of structural vibrations. Using this method, Smith [33] has shown significant improvement over a pure rigid-body based design. However, the notch filters have an adverse effect on the loop phase, and do not completely eliminate the structural vibrations due to external disturbances or modeling uncertainties. Conversely, active vibration damping can result in better performance by attenuating the structural resonances using feedback.

Chen and Tlusty proposed a method for active vibration damping using accelerometer feedback and showed its effectiveness in simulations [6]. As computer processors and feedback resolution have improved, successful experimental results have been reported by several researchers. Symens et al. [34] used H_∞ control with gain scheduling to account for the position dependency of the structural vibrations. Zatarain et al. [43] combined linear encoder and accelerometer feedback using a Kalman filter to improve drive stiffness and damping. Another approach, presented by Schäfers [31], is to tune the proportional-integral controlled velocity loop to emulate a vibration absorber. Kamalzadeh and Erkorkmaz [19] have developed an adaptive sliding mode controller (ASMC) for active vibration damping which actively compensates for the dynamics of the 1st axial mode of a ball screw drive. The disturbance adaptive discrete-time sliding mode controller (DADSC) proposed by Won and Hedrick [41] has been extended by Altintas and Okwudire to actively compensate for the axial mode in ball screw drives [25] and for damping of structural vibrations in direct feed drives [2].

Recently, Gordon and Erkorkmaz have developed a method of actively damping the axial mode in ball screw drives using a pole-placement controller [15]. The most crucial step in pole-placement controller design is the choice of desired closed-loop pole locations. Some insight into desirable pole locations for suppressing the axial vibrations comes from the concept of low authority control, as described in [12]. Low authority control seeks to suppress resonance peaks while minimally affecting the transfer function away from the resonance. In the root-locus, this corresponds to a change in the real part of the complex poles, without significantly changing the imaginary part. When the closed-loop pole locations have been chosen, the feedback gains can be calculated using Ackermann's formula [10][24] or other more robust pole-placement algorithms [20].

Teo et al. [35] have reported successful experimental results on a ball screw driven gantry using adaptive control based on rigid body dynamics. Weng et al. [40] have proposed the concept of sensor and actuator averaging for controlling flexible structures, in particular beams and plates. The sensor/actuator averaging acts as a spacial filter and can be used to attenuate resonances without the phase penalty associated with

notch filtering. This concept has been extended by Gordon and Erkorkmaz [14] to control a linear motor driven gantry, which is presented in Chapter 4.

2.3 Feedforward Control

Feedforward control can be used to enhance command tracking, as well as avoid excitation of structural resonances. However, feedforward control is sensitive to the accuracy of the underlying model and not robust against disturbances or changes in the plant [30]. Before applying feedforward control, closed-loop robustness should be realized through feedback control.

It is common practice to make a feedforward controller approximate the inverse of the plant in order to minimize the transfer function from the reference to the error. However, model inversion is not always possible, notably in systems with non-minimum phase (unstable) zeros. Since many systems are dominated by rigid-body behavior, use of acceleration feedforward is widespread. Acceleration feedforward generates a control signal equal to the modeled mass times the commanded acceleration. For many systems, applying this scheme leaves an error profile with correlated to the derivatives of acceleration. Boerlag et al. [5] have extended acceleration feedforward to the derivative of jerk (i.e., snap), in order to compensate for the residual servo errors. A new method of removing these artifacts through trajectory pre-filtering was also developed by Gordon and Erkorkmaz in [15]. This approach is detailed in Chapter 3, and has been used in both Chapter 3 and Chapter 4

Tomizuka [36] developed the zero phase error tracking controller (ZPETC) to cancel out the poles and stable zeros of a closed-loop system, and approximately cancel out the non-minimum phase zeros. This theoretically results in a zero phase lag and unity gain for a wide frequency range. Others, including Weck and Ye [39], have also developed similar techniques. These methods result in non-causal systems.

Feedforward control can be used to avoid exciting structural vibrations. One such technique that has been demonstrated is input command pre-shaping (ICP) or input shaping. Based on a dynamic model of the system, ICP generates a series of impulses such that the oscillatory parts of the impulse response cancel out, allowing vibration free positioning to be achieved [16]. Jones and Ulsoy [17] found that ICP was a special case of notch filtering the position commands, and have successfully applied this strategy o controlling coordinate measuring machines (CMM's).

2.4 Conclusions

This chapter has presented a review of the work done previously in areas related to the thesis topic. The various approaches to modeling and control of machine tool feed drives have been presented. In general, the approach used in this thesis has been to make use of the simplest tools available which still provide effective results.

Chapter 3
Control of Ball Screw Drives

3.1 Introduction

In this chapter, pole-placement control is used to actively dampen the 1st mode of axial vibrations in a ball screw drive. Trajectory tracking is improved through feedforward control, using inverted plant dynamics, feedforward friction compensation, and a Least Squares tuned trajectory pre-filter. Effectiveness of the proposed strategy is verified in frequency domain analyses and also in rope-snap testing, and trajectory tracking and metal cutting experiments. The proposed scheme is compared to the mainstream P-PI cascade design used in industry.

3.2 Controller Design

The proposed overall control scheme is shown in Figure 3.1. The feedback loop is closed using pole-placement control, which provides active vibration damping for the axial mode, as well as motion control. Feedforward terms, including inverted system dynamics and Stribeck-type friction compensation are included in order to improve command tracking. A new trajectory pre-filter has been developed, which removes the artifacts of the commanded velocity, acceleration, jerk and snap from the tracking error. Finally, a filter pack comprising of notch and low-pass filters is added to ensure stability. In the following subsections, the purpose and design of the individual components will be explained. Their individual contributions will be validated through frequency domain analyses in Section 3.3 and shown in experimental results in Section 3.4.
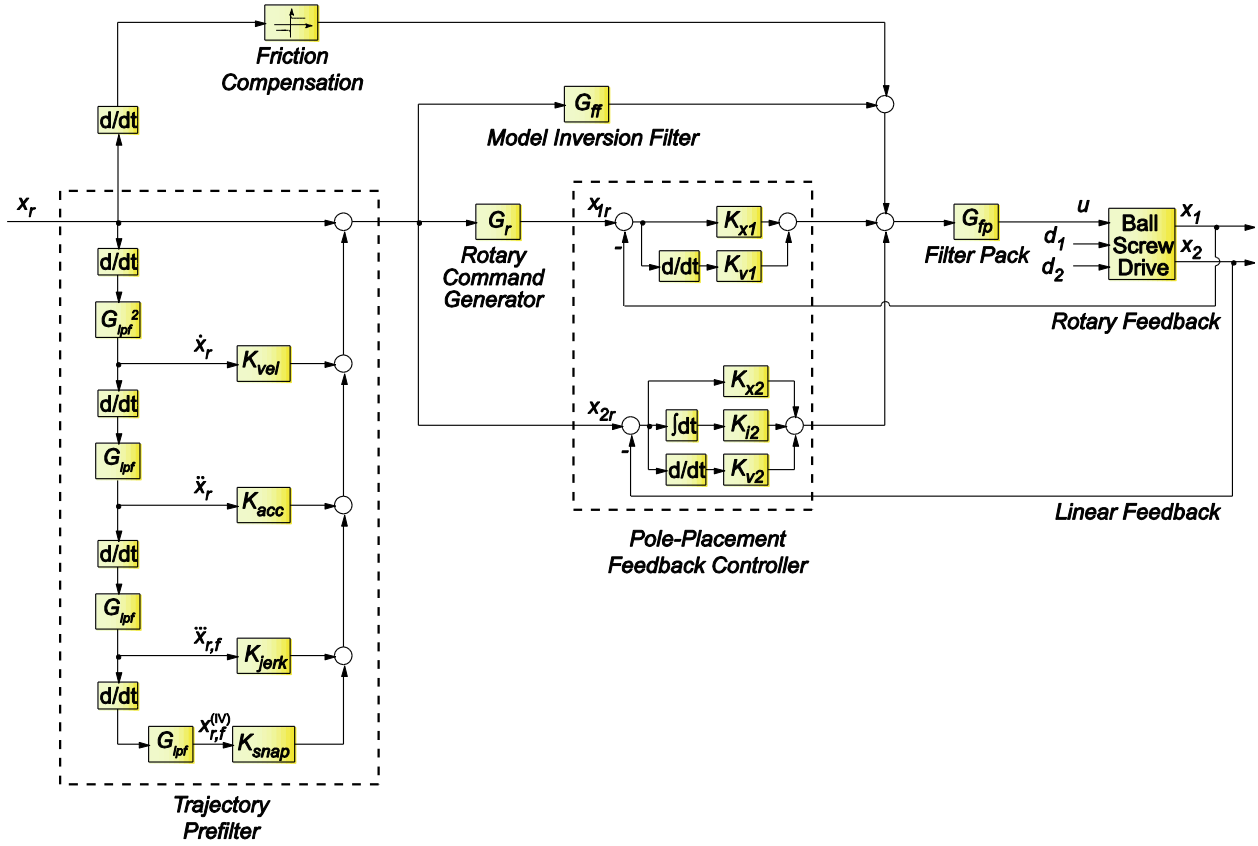
Figure 3.1: Proposed control scheme which compensates the 1st axial mode using pole-placement.

3.2.1 Drive Model

The ball screw drive test bed is shown in Figure 3.2. The table is supported by an air guideway system and driven by an NSK W2010FA-3P-C5Z20 precision ball screw with 20 mm pitch and 20 mm diameter. A 3 kW AC servomotor provides the actuation through a diaphragm type coupling. Feedback is provided by a high resolution rotary encoder which is mounted on the ball screw and a linear encoder mounted on the table. The rotary encoder produces 5000 sinusoidal signals per revolution which can be interpolated by 400 times, giving a position measurement resolution equivalent to 10 nm of table motion. The catalogue rated accuracy of this encoder is equivalent to 200 nm of table motion. The linear encoder, which has a rated accuracy of 40 nm, has 4 um signal period and is also interpolated 400 times, providing a measurement resolution of 10 nm. The control laws are implemented at 20 kHz sampling frequency on a dSpace system.

9
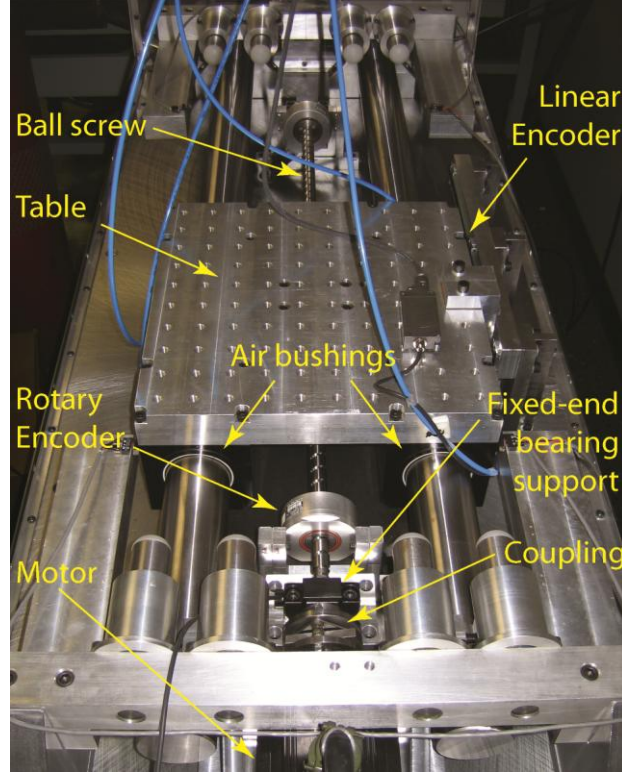
Figure 3.2: Ball screw drive setup.
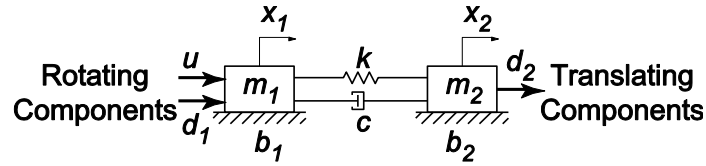
Figure 3.3: Simplified flexible drive model.

The controller is designed considering the simplified dynamic model shown in Figure 3.3, which is captured by Equation (3.1):

$$m_1\ddot{x}_1 = -b_1\dot{x}_1 + k(x_2 - x_1) + c(\dot{x}_2 - \dot{x}_1) + u + d_1$$
$$m_2\ddot{x}_2 = -b_2\dot{x}_2 + k(x_1 - x_2) + c(\dot{x}_1 - \dot{x}_2) + d_2 \qquad (3.1)$$

As shown in earlier work [19], this model captures the dynamics of the 1st axial mode with sufficient closeness. If necessary, more accurate models can also be used with the proposed PPC scheme, such as those presented in [25][38] which have a full mass matrix and take the form,

10

$$\begin{bmatrix} m_{11} & m_{12} \\ m_{12} & m_{22} \end{bmatrix} \ddot{\mathbf{x}} + \begin{bmatrix} c_{11} & c_{12} \\ c_{12} & c_{22} \end{bmatrix} \dot{\mathbf{x}} + \begin{bmatrix} k & -k \\ -k & k \end{bmatrix} \mathbf{x} = \mathbf{F} \tag{3.2}$$

In Figure 3.3, the inertias of the rotating and translating components are denoted by m_1 and m_2. k represents the overall axial stiffness, which is influenced by the nut, the fixed bearing, and torsional and axial stiffness of the screw. The damping in the preloaded nut is represented by c. Viscous damping at the motor and screw bearings, and table guideways, is captured with b_1 and b_2. The motor torque is represented in terms of the equivalent control signal u [V]. d_1 and d_2 correspond to equivalent disturbances acting on the rotating and translating components. The position units are radians, which represent equivalent rotational motion of the screw. The identified control signal equivalent parameters are shown in Table 3.1.

Table 3.1: Identified parameters

Parameter	Identified Value	Units
m_1	1.858×10^{-3}	$V/(rad/s^2)$
m_2	0.379×10^{-3}	$V/(rad/s^2)$
b_1	1.020×10^{-3}	$V/(rad/s)$
b_2	0	$V/(rad/s)$
k	210.02	V/rad
c	0.014	$V/(rad/s)$

This model was validated by comparing the acceleration FRF measured through the rotary and linear encoders with the model FRF, as shown in Figure 3.4a. As can be seen, the 1st axial mode at 130 Hz is adequately captured. However, the gain and phase agreement deteriorates after ~250 Hz due to additional dynamics contributed by the torsional modes (440, 1100 Hz), and the bandwidth of the drive's current control loop, which was identified to be 450 Hz. The identified drive model comprises of complex conjugate poles $(s_{1,2} = -\sigma_1 \pm j\omega_{d1})$ at 130 Hz with 2.7% damping, a real pole at 0.07 Hz due to the interaction of viscous friction with the total inertia, and an integrator for velocity to position conversion.
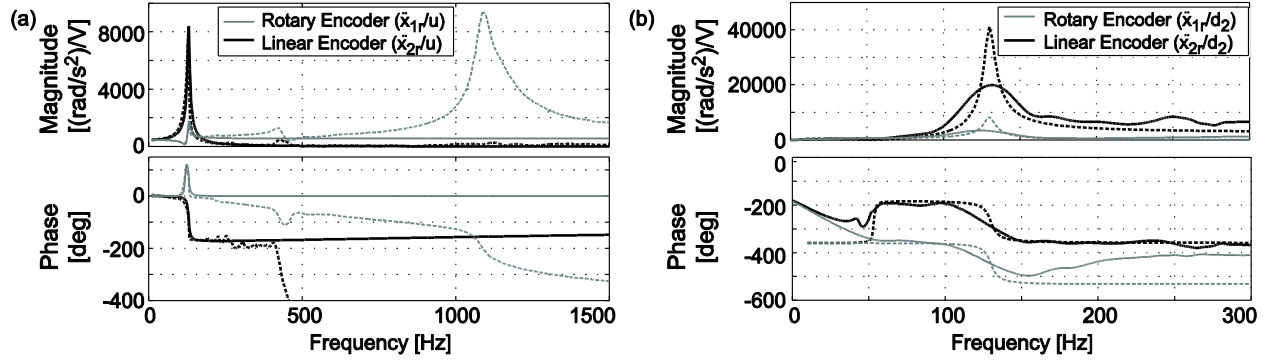
Figure 3.4: Measured and modeled drive FRF's with (a) excitation from motor and (b) excitation from impact hammer.

The disturbance response of the drive was measured through impact hammer testing and is shown compared to the model response in Figure 3.4b. A small resonance at 43 Hz is noted in the disturbance FRF. Further testing revealed that this mode corresponded to the pitching motion of the table on the cylindrical guideways. The ball screw was mounted at the same level as the guideways; hence this mode cannot be excited by the motor and therefore it is not considered in the controller design. However, it does appear in the disturbance response observed in the experimental results. The discrepancy between the modeled and measured disturbance response is postulated to be due to the lack of excitation provided by the small instrumented hammer used for this measurement. Further investigation with a larger hammer is planned.

To gauge the position dependency of the ball screw's response, FRF measurements were taken, with the excitation from the motor, spanning most of the travel range of the ball screw at 0, 150 and 300 mm. As seen in Figure 3.5, the frequency response of the drive does not vary significantly with table position. However, for ball screw drives with heavier tables or a longer stroke, the variation may become significant and a gain scheduling method may be required, as implemented in [27][34].

12
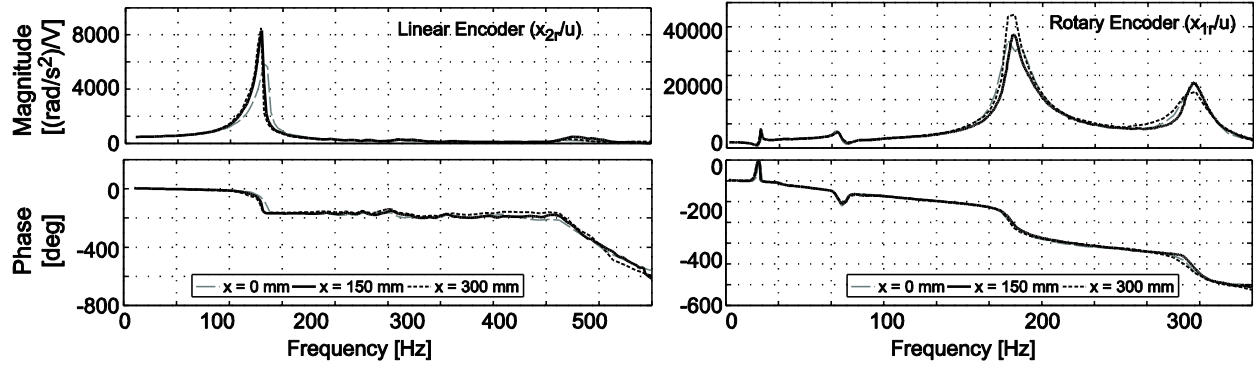
Figure 3.5: Variation of system FRF with table position.

3.2.2 Pole-Placement Feedback Design

The equations of motion in Equation (3.1) can also be represented in state-space:

$$\dot{\mathbf{z}} = \mathbf{A}\mathbf{z} + \begin{bmatrix} \mathbf{B}_1 & \mathbf{B}_2 & \mathbf{B}_3 \end{bmatrix} \begin{bmatrix} u \\ d_1 \\ d_2 \end{bmatrix} \quad , \quad \begin{bmatrix} x_1 \\ x_2 \end{bmatrix} = \mathbf{C}\mathbf{z} \tag{3.3}$$

Where

$$\mathbf{A} = \begin{bmatrix} 0 & 0 & 1 & 0 \\ 0 & 0 & 0 & 1 \\ -k/m_1 & k/m_1 & -(c+b_1)/m_1 & c/m_1 \\ k/m_2 & -k/m_2 & c/m_2 & -(c+b_2)/m_2 \end{bmatrix},$$

$$\mathbf{B}_1 = \begin{bmatrix} 0 \\ 0 \\ 1/m_1 \\ 0 \end{bmatrix}, \quad \mathbf{B}_2 = \begin{bmatrix} 0 \\ 0 \\ 1/m_1 \\ 0 \end{bmatrix}, \quad \mathbf{B}_3 = \begin{bmatrix} 0 \\ 0 \\ 0 \\ 1/m_2 \end{bmatrix}$$

and also in transfer function matrix form:

$$\begin{bmatrix} x_1 \\ x_2 \end{bmatrix} = \begin{bmatrix} G_{11} & G_{12} & G_{13} \\ G_{21} & G_{22} & G_{23} \end{bmatrix} \begin{bmatrix} u \\ d_1 \\ d_2 \end{bmatrix} \tag{3.4}$$

13

where

$$G_{11} = \frac{x_1}{u} = G_{12} = \frac{x_1}{d_1} = \frac{m_2 s^2 + (c+b_2)s + k}{m_1 m_2 s^4 + a_1 s^3 + a_2 s^2 + a_3 s} \qquad G_{13} = \frac{x_1}{d_2} = \frac{cs + k}{m_1 m_2 s^4 + a_1 s^3 + a_2 s^2 + a_3 s}$$

$$G_{21} = \frac{x_2}{u} = G_{22} = \frac{x_2}{d_1} = \frac{cs + k}{m_1 m_2 s^4 + a_1 s^3 + a_2 s^2 + a_3 s} \qquad G_{23} = \frac{x_2}{d_2} = \frac{m_1 s^2 + (c+b_1)s + k}{m_1 m_2 s^4 + a_1 s^3 + a_2 s^2 + a_3 s}$$

and

$$a_1 = m_1 b_2 + m_2 b_1 + (m_1 + m_2)c$$
$$a_2 = b_1 b_2 + (b_1 + b_2)c + (m_1 + m_2)k$$
$$a_3 = (b_1 + b_2)k$$

The states to be controlled are the position and velocity of the rotating and translating components. The position values are practically measureable, and the velocity estimates can be obtained using backwards Euler approximation,

$$\hat{\dot{x}}_{1,k} = \frac{x_{1,k} - x_{1,k-1}}{T_s}, \quad \hat{\dot{x}}_{2,k} = \frac{x_{2,k} - x_{2,k-1}}{T_s} \tag{3.5}$$

It is also desirable to eliminate steady-state positioning errors on the nut side due to unmodeled disturbances and dynamic effects such as the motion loss in the preloaded nut [7], which cannot be captured with the linear model in Figure 3.3. Thus, the integrated table position, $x_{2i} = \int x_2(t)dt$, is also considered as an additional state to be controlled, resulting in the state vector to become,

$$\mathbf{z} = \begin{bmatrix} x_1 & x_2 & \dot{x}_1 & \dot{x}_2 & x_{2i} \end{bmatrix}^T \tag{3.6}$$

The feedback controller is designed principally through the use of pole-placement control (PPC) [23]. The objective is to increase the dynamic stiffness of the ball screw around the 1st axial mode, while also realizing a sufficiently high tracking and disturbance rejection bandwidth for rigid body dynamics. The model has 5 states; hence, 5 pole locations are required. Two of the poles $(p_{1,2})$ are placed to speed up the decay of axial vibrations without altering their oscillation frequency. This is similar to the idea of low authority LQG vibration control [12]. A change in the vibration frequency would be more costly in terms of control effort, since these poles originate from the drive's mechanical structure. Hence, only the real component $-\sigma_1$ is shifted further to the left in the s-plane as,

14

$$p_{1,2} = -\beta\sigma_1 \pm j\omega_{d1}, \text{ where } \beta \geq 1 \tag{3.7}$$

In our setup, β could be increased up to $\beta = 4$. The remaining three poles, which relate to the rigid body motion interacting with the servo controller, which has integral action, are placed at a reasonably high frequency which will yield good disturbance rejection and tracking without significantly jeopardizing the stability margins. They were chosen to have a pole frequency of $\omega_2 = 50\,\text{Hz}$ with two of the poles being complex with $\zeta_2 = 0.7$ damping. Hence,

$$\begin{aligned} p_{3,4} &= -\zeta_2\omega_2 \pm j\omega_2\sqrt{1-\zeta_2{}^2} \\ p_5 &= -\omega_2 \end{aligned} \tag{3.8}$$

The state feedback gain $\mathbf{K} = \begin{bmatrix} K_{x1} & K_{x2} & K_{v1} & K_{v2} & K_{i2} \end{bmatrix}$ is computed to achieve $\mathrm{eig}(\mathbf{A} - \mathbf{B_1 K}) = \{p_1 \ldots p_5\}$. Ackermann's formula could be used [24], but standard algorithms in software such as Matlab® can also be applied, giving more robust results. The open- and closed-loop pole locations are illustrated in Figure 3.6.
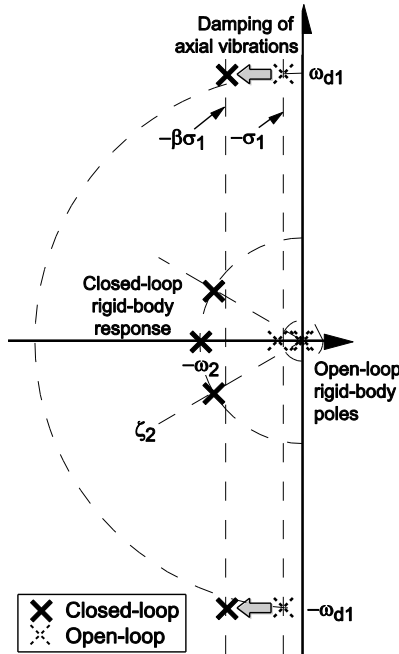
Figure 3.6: Open- and closed-loop pole locations.

15

In practical implementation, additional dynamics due to torsional modes of the ball screw and the motor current loop cause noticeable discrepancies between the modeled and actual drive response after 250 Hz. These can result in serious stability problems unless their effect is attenuated, which is generally achieved using low-pass filters. However, since the torsional modes exhibit very little variation with table position and remain constant over the prolonged use of the ball screw, they can be attenuated with notch filters in the form:

$$G_{notch}(s) = \prod_{k=1}^{2} \left(\frac{s^2 + 2\zeta_{zk}\omega_{n,k}s + \omega_{n,k}}{s^2 + 2\zeta_{pk}\omega_{n,k} + \omega_{n,k}} \right) \tag{3.9}$$

with $\omega_{n,1} = 420\,\text{Hz}$ ($\zeta_{z1} = 0.55$, $\zeta_{p1} = 0.7$) and $\omega_{n,2} = 1080\,\text{Hz}$ ($\zeta_{z2} = 0.05$, $\zeta_{p2} = 0.7$). Notch filters cause smaller phase loss compared to low-pass filters, allowing a higher crossover frequency to be achieved. High frequency dynamics beyond the first two torsional modes are attenuated with a low-pass filter with a pole frequency of $\omega_{lpf} = 2000$ Hz. The combined transfer function of the filter pack shown in Figure 3.1 can be expressed as:

$$G_{fp}(s) = \frac{\omega_{lpf}}{s + \omega_{lpf}} \cdot G_{notch}(s) \tag{3.10}$$

3.2.3 State Trajectory Generation and Model Inversion

Following the feedback design, feedforward terms are designed to improve the command tracking. Since the command x_r corresponds to the desired table motion (x_{2r}), the flexibility of the ball screw must be considered when generating the motion commands for the ball screw's rotary motion. This is achieved by the rotary command generator, $G_r(s)$ in Figure 3.1. Solving Equation (3.2) for x_2 results in:

$$x_2(s) = \frac{cs + k}{m_2 s^2 + (b_2 + c)s + k} x_1(s) + d_2(s) \tag{3.11}$$

If d_2 is ignored, $G_r(s) = x_1/x_2$ becomes,

$$G_r(s) = \frac{m_2 s^2 + (b_2 + c)s + k}{cs + k} \tag{3.12}$$

16

which determines the necessary rotational motion of the screw to accommodate the desired table motion (x_{2r}).

Additional feedforward action is provided by inverting the plant dynamics G_{21} from the control signal input (u) to the table linear position (x_2). Hence, the model inversion filter G_{ff} in Figure 3.1 becomes:

$$G_{ff}(s) = \frac{m_1 m_2 s^4 + a_1 s^3 + a_2 s^2 + a_3 s}{cs + k} \tag{3.13}$$

The denominator coefficients a_1, a_2 and a_3 have been defined in Equation (3.4). In real-time implementation, G_{ff} and G_r were discretized using pole-zero matching [24] and adding the necessary delay terms to make them causal.

3.2.4 Trajectory Pre-filtering

When the ideal plant and s-domain controllers are considered, the control signal can be expressed as:

$$u(s) = \frac{G_{ff} + K_1 G_r + K_2}{1 + K_1 G_{11} + K_2 G_{21}} x_r(s), \text{ where } \begin{array}{l} K_1(s) = (K_{x1} + K_{v1}s)G_{fp} \\ K_2(s) = (K_{x2} + K_{i2}/s + K_{v2}s)G_{fp} \end{array} \tag{3.14}$$

By substituting the expression for u in Equation (3.14) into the expression for G_{21} from Equation (3.4):

$$x_2 = G_{21}u = \frac{G_{ff}G_{21} + K_1 \overbrace{G_r G_{21}}^{G_{11}} + K_2 G_{21}}{1 + K_1 G_{11} + K_2 G_{21}} x_r \tag{3.15}$$

It can be seen that the overall tracking transfer function, from the trajectory command to the table translational motion, simplifies to $x_2/x_r = 1$. However, due to computational delays, sampling, and variation of the actual drive FRF from the ideal model, the tracking transfer function will be distorted. As a result, artifacts correlated to the velocity, acceleration, jerk and snap commands may appear in the tracking error profile, as was experimentally observed and presented in Figure 3.7. To address this problem, a new type of trajectory pre-filter has been designed, as shown in Figure 3.1.

17
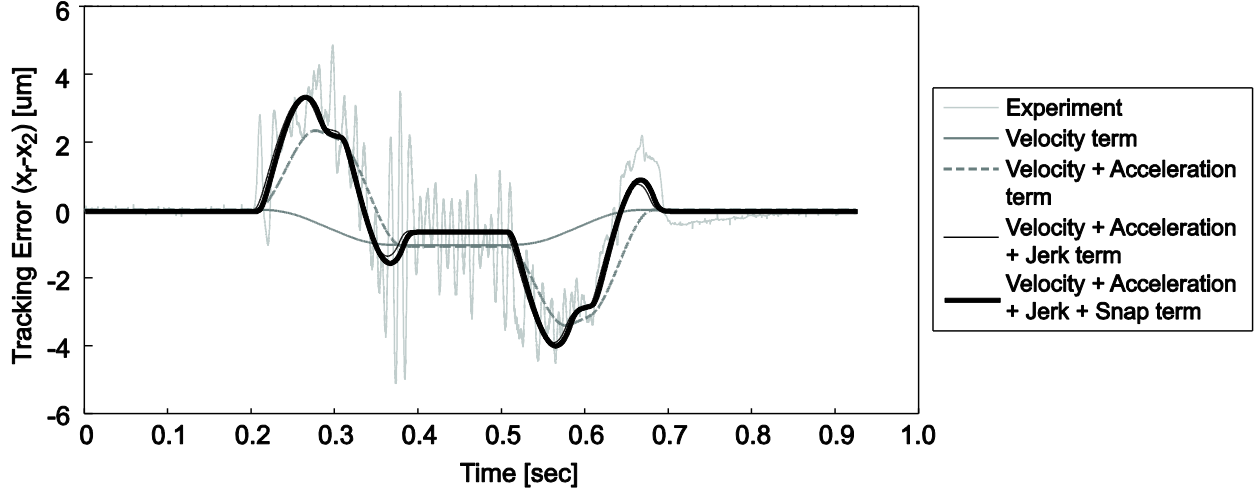
Figure 3.7: Tracking error profile with velocity, acceleration, jerk and snap artifacts.

The actual distorted version of x_2/x_r will be referred to as G_{track}. The error transfer function, $G_e = 1 - G_{track}$, is defined such that the observed translational tracking error can be obtained as $e_2 = G_e x_r$. As can be seen from Figure 3.7, the tracking error appears to be correlated with the velocity, acceleration, jerk and snap profiles through a quasi-static (steady-state) relationship. Hence, expanding the Maclaurin series for $G_e(s)$ around zero frequency $(s = 0)$ yields:

$$G_e(s) = G_e(0) + G_e'(0)s + \frac{1}{2!}G_e''(0)s^2 + \frac{1}{3!}G_e'''(0)s^3 + \frac{1}{4!}G_e^{(IV)}(0)s^4 + \dots \qquad (3.16)$$

where G_e', G_e'', G_e''' and $G_e^{(IV)}$ are the first four derivatives of G_e with respect to s. Since G_{track} has been designed to yield zero steady state error to position commands, $G_e(0) = 0$. Also, since there are no integrators in G_e, the derivative terms will all be finite at $s = 0$. Thus, G_e can be estimated for low frequencies by identifying the first four nonzero terms of Equation (3.16),

$$\hat{G}_e = K_{vel}s + K_{acc}s^2 + K_{jerk}s^3 + K_{snap}s^4 \qquad (3.17)$$

The coefficients $K_{vel} = G_e'(0)$, $K_{acc} = G_e''(0)/2!$, $K_{jerk} = G_e'''(0)/3!$, and $K_{snap} = G_e^{(IV)}(0)/4!$ are computed using the Least Squares technique to allow the prediction of e_2 as a function of the filtered commanded kinematic profiles:

18

$$\hat{e}_2 = K_{vel}\dot{x}_{rf} + K_{acc}\ddot{x}_{rf} + K_{jerk}\dddot{x}_{rf} + K_{snap}x_{rf}^{(IV)}$$ (3.18)

Filtering is used, as shown in Figure 3.1, in order to avoid numerical problems with high order derivatives. The low-pass filter, G_{lpf}, which is employed multiple times, was designed to be 1st order with a pole frequency of 80 Hz. The filtered velocity, acceleration, jerk and snap commands are obtained as,

$$\dot{x}_{rf}(s) = G_{lpf}^{\,2}(s) \cdot \dot{x}(s)$$
$$\ddot{x}_{rf}(s) = G_{lpf}^{\,3}(s) \cdot \ddot{x}(s)$$
$$\dddot{x}_{rf}(s) = G_{lpf}^{\,4}(s) \cdot \dddot{x}(s)$$
$$x_{rf}^{(IV)}(s) = G_{lpf}^{\,5}(s) \cdot x^{(IV)}(s)$$ (3.19)

A single tracking experiment, with the gains K_{vel}, K_{acc}, K_{jerk}, and K_{snap} set to zero, is sufficient to identify the filter coefficients. The resulting model allows adequate prediction of the tracking error, shown in Figure 3.7.

If the commanded trajectory is offset by the predicted error,

$$x'_r = x_r + \hat{G}_e x_r = (1+\hat{G}_e)x_r$$ (3.20)

the table position becomes,

$$x_2 = G_{track}x'_r = G_{track}(1+\hat{G}_e)x_r$$ (3.21)

Using this result, the tracking error is now,

$$\begin{aligned} e_2 &= x_r - x_2 \\ &= x_r - G_{track}(1+\hat{G}_e)x_r \\ &= (1 - G_{track} - G_{track}\hat{G}_e)x_r \\ &= (G_e - G_{track}\hat{G}_e)x_r \end{aligned}$$ (3.22)

For low frequencies, assuming that the approximation $\hat{G}_e \cong G_e$ holds:

19

$$e_2 = (1 - G_{track})G_e x_r = G_e{}^2 x_r \qquad (3.23)$$

Equation (3.23) shows that the tracking error is reduced for frequencies where $|G_e| < 1$. In particular, this effect is realized at low frequencies where $|G_{track}|$ is designed to be close to one ($|G_e| \ll 1$). For example, if $|G_e(j\omega_0)| = 0.1$, the theoretical command following error at frequency ω_0 will be reduced further by a factor of 10 due to the addition of the trajectory pre-filter.

3.3 Frequency Domain Analyses

Although the system has two outputs, the fact that there is only one controlled input allows SISO-type frequency domain analyses to be carried out. The following frequency domain concepts are used throughout the controller design, tuning and evaluation steps.

Loop Transfer Function

Given the plant, $G(s)$, and the feedback controller, $K(s)$, the loop transfer function is $L(s) = G(s)K(s)$. The bandwidth of a closed-loop system can be approximated by the crossover frequency, which is frequency at which $|L(j\omega)| = 1$.

Nyquist Stability Criterion

The Nyquist criterion provides a method for determining the closed-loop stability of a system. For a stable open-loop system, if the locus of the loop transfer function, $L(s)$, plotted from $s = -j\infty$ to $s = +j\infty$ makes no net encirclements of the point $s = -1$, the closed-loop system is stable.

Sensitivity Function

The sensitivity function is $S(j\omega) = 1/(1 + L(j\omega))$. The magnitude of the sensitivity function corresponds to the inverse of the distance from the Nyquist plot to the critical "-1" point. Thus, the sensitivity function is a useful measure of stability margins, and in practice, it is desirable to keep its maximum value, $M_S = \max_{\omega} |S(j\omega)| = \|S\|_\infty$, below 1.5-2.5. Also, the controller actively rejects input-level disturbances for frequencies at which $|S(j\omega)| < 1$.

In the analyses, three cases are considered:

20

(a) ideal modeled plant and continuous time (s-domain) controller,

(b) experimentally measured plant and s-domain controller,

(c) experimentally measured plant and discrete time (z-domain) controller.

The discretized version of the control law includes the phase delay effects of the zero-order hold and a full sample (i.e., worst case) computational delay, at a sampling frequency of 20 kHz.

Considering Figure 3.8, the loop transfer function for the mode compensating pole-placement controller (MC-PPC) can be expressed as:

$$L = K_1 G_{11} + K_2 G_{21} \tag{3.24}$$

K_1 and K_2 were defined in Equation (3.14) and G_{11} and G_{21} were defined in Equation (3.4).
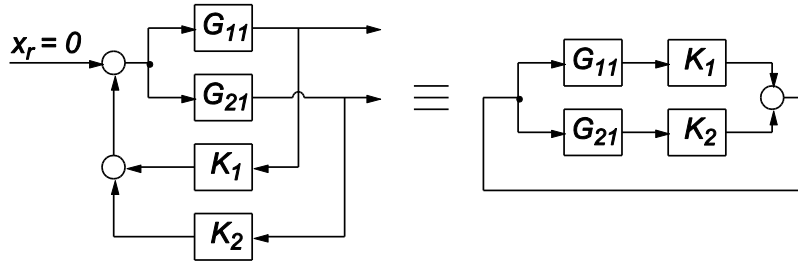
Figure 3.8: Block diagram manipulation for assessing closed-loop stability.

In order to demonstrate the effectiveness of the developed MC-PPC, it has been compared to the well-established P-PI position-velocity cascade controller that is commonly used on feed drives in industry. The P-PI scheme is shown in Figure 3.9.
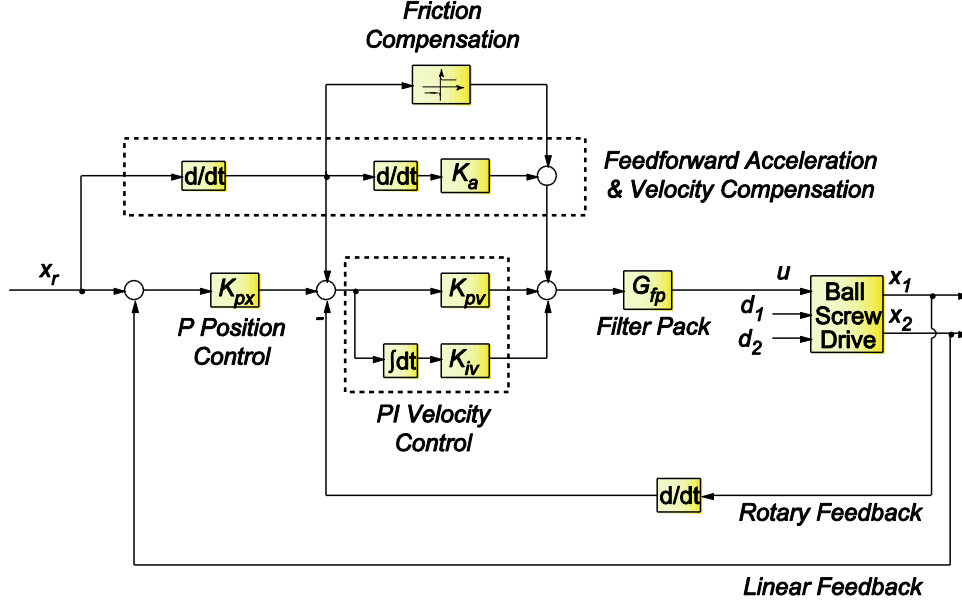
Figure 3.9: P-PI position-velocity cascade control scheme with velocity and acceleration feedforward terms.

To allow for a fair comparison, the MC-PPC and P-PI controllers were tuned to possess similar stability margins using frequency domain analyses. Both controllers have phase margins of $PM \cong 30°$ and maximum sensitivity values $S_{max} \leq 3.25$. These stability margins are slightly more aggressive than commonly used values, favoring tracking accuracy over robustness in order to evaluate the best possible performance that could be achieved with both controllers. In practical implementation, both controllers can be detuned as required in order to yield better stability margins. The filter pack, G_{fp}, and the feedforward friction compensation are implemented in an identical fashion for both controllers.

The loop transfer function for the P-PI controlled system can be found to be:

$$L = G_{fp} \frac{K_{pv}s + K_{iv}}{s}(G_{11}s + G_{21}K_{px})$$
(3.25)

By inspecting the loop magnitude plots in Figure 3.10ab, the frequency domain results suggest that the MC-PPC will have superior tracking and disturbance rejection, as it has significantly higher low frequency gain and achieves higher crossover frequencies of 100 and 170 Hz, compared to 70 and 134 Hz

22

for the P-PI. The 2nd crossover frequency with $|L(j\omega)| > 1$ indicates the frequency range up to which the controller is actively damping the axial vibrations.
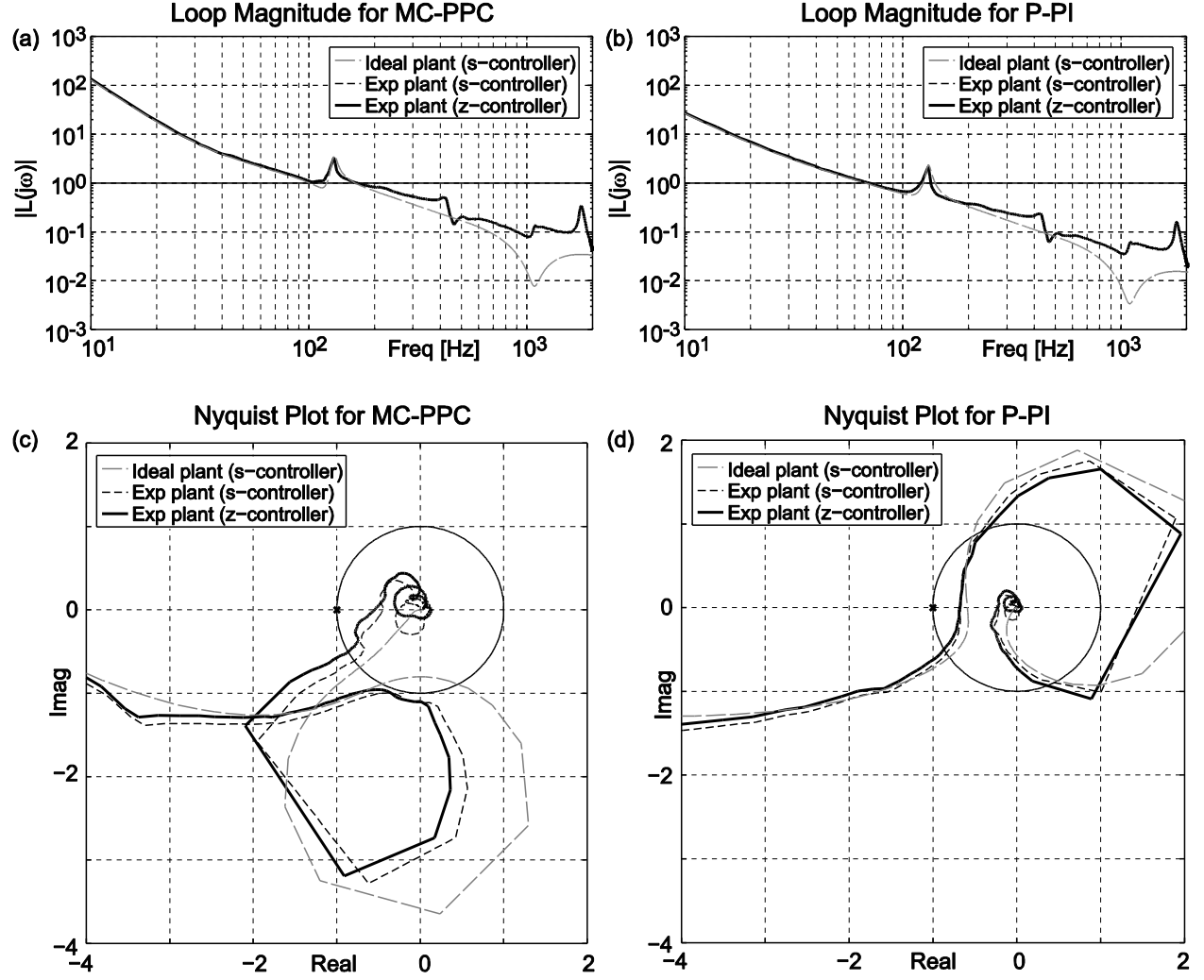
Figure 3.10: Loop magnitude of (a) MC-PPC and (b) P-PI; Nyquist plot for (c) MC-PPC and (d) P-PI.

The sensitivity plots for the two controllers are shown in Figure 3.11. Interestingly, the MC-PPC peak sensitivity value increases from 2.35 with the s-domain controller to 3.04 for the discretized version. Thus, a higher sampling frequency beyond 20 kHz could yield a significant improvement in the stability margins for this controller. On the other hand, the P-PI peak sensitivity only increases from $|S|_{max} = 3.04$ for the continuous time controller to 3.25 for the z-domain controller. This suggests the performance is

23

primarily limited not as a result of the effect of sampling, but rather due to the control structure which considers only the rigid body plant. Also, $|S| < 1$ for 0-134 Hz for the MC-PPC, compared to only 0-46 Hz and 120-146 Hz for the P-PI controller. This indicates a larger disturbance rejection bandwidth for the MC-PPC.
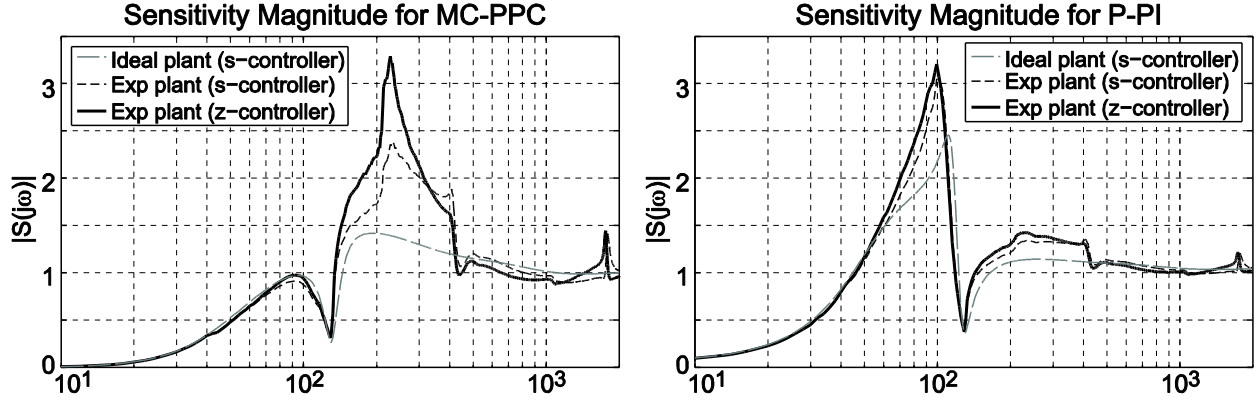
Figure 3.11: Sensitivity magnitude for (a) MC-PPC and (b) P-PI.

The open-loop transfer function from table disturbances, d_2 (e.g., cutting forces), to the table position, x_2, is given in Equation (3.4) as G_{23}. The closed-loop disturbance transfer function for the system controlled by the MC-PPC can be obtained as:

$$G_{d_2 \to x_2} = \frac{G_{23} + K_1(G_{11}G_{23} - G_{13}G_{21})}{1 + L} \tag{3.26}$$

For the system controlled by the P-PI controller, the disturbance transfer function is:

$$G_{d_2 \to x_2} = \frac{G_{23} + G_{fp}(K_{pv}s + K_{iv})(G_{11}G_{23} - G_{13}G_{21})}{1 + L} \tag{3.27}$$

By analyzing the disturbance transfer functions in Figure 3.12, it can be seen that active damping yields improved disturbance rejection. The maximum negative real value of the disturbance transfer function is 0.0083 rad/V at 145 Hz for the MC-PPC and 0.014 rad/V at 126 Hz for the P-PI. This indicates an improvement in the drive's immunity to machining chatter vibrations [3].

24
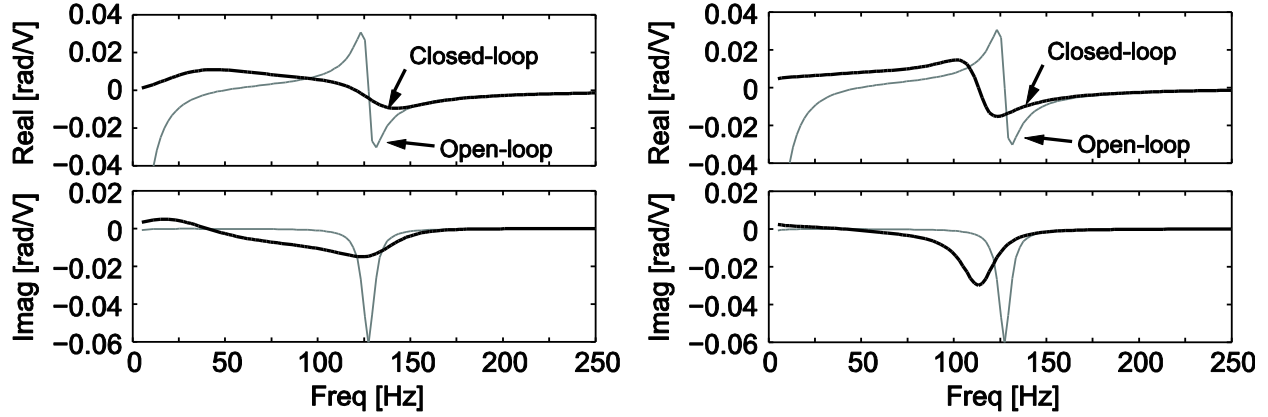
Figure 3.12: Disturbance transfer functions for MC-PPC (left) and P-PI (right) considering ideal plant.

The ideal closed-loop tracking transfer function has a unity gain and zero phase. As can be seen in Figure 3.13, the feedforward terms significantly improve the tracking performance of the drive. The inertia and viscous friction compensation flattens both the gain and phase up to around 100 Hz. However, discretization and computational delay cause distortion in the phase and, to a lesser degree, the magnitude. The pre-filter helps to mitigate this effect, reducing the phase lag up to ~120 Hz and bringing the magnitude close to unity up to ~80 Hz.
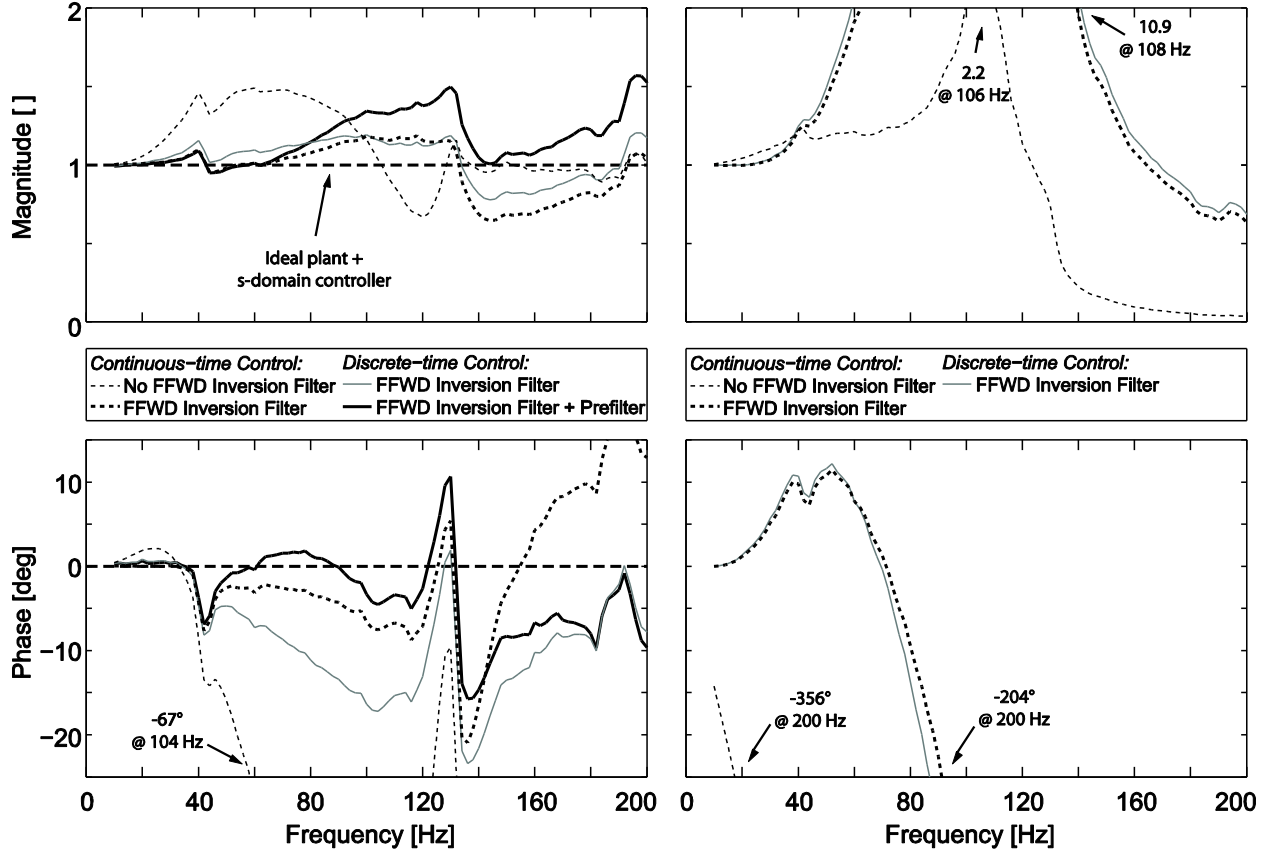
Figure 3.13: Command tracking with MC-PPC (left) and P-PI (right) with experimentally measured plant

3.4 Experimental Results

The performance of the MC-PPC was compared to the P-PI controller in experiments.

The superior disturbance rejection capability of the MC-PPC can be seen in the results of rope snap (step disturbance) tests. As shown in Figure 3.14, the MC-PPC has a lower peak displacement due to its higher control bandwidth, and a much better rejection of the low-frequency disturbance as seen in the faster return of the rigid-body to zero displacement. The decay of the 43 Hz vibrations is also much quicker, as the MC-PPC has a 5 percent settling time of 0.203 seconds, compared to 0.632 seconds for the P-PI controller. By comparing the amplitude spectral densities [22] in Figure 3.14b, it is seen that the MC-PPC step disturbance response has smaller low-frequency amplitudes, as is expected given the larger low frequency gain seen in Figure 3.10a. The peak at 43 Hz corresponds to the pitching mode of the table, as discussed in Section 3.2.1.

26
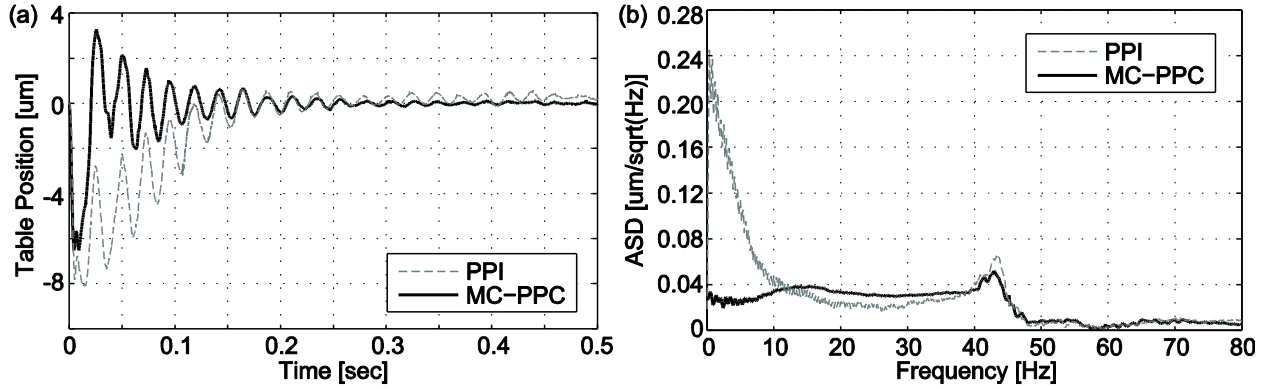
Figure 3.14: (a) Table displacement and (b) amplitude spectral density of table displacement for the MC-PPC and P-PI in Rope Snap Test

High speed tracking tests at 200, 500 and 1000 mm/s were conducted in order to validate the performance of the controller. Each test was repeated 5 times, and average results are shown in Figure 3.15abc. The MC-PPC significantly outperforms the P-PI both during constant velocity and during acceleration transients as indicated by the lower RMS and maximum errors in Table 3.2.

Furthermore, the controller performance was verified in metal cutting tests. Tests were performed at 200 mm/s while performing a slotting operation with a 4 flute 25.4 mm end mill in 6065 aluminum. The spindle speed was 3500 rpm and depth of cut was 0.2 mm. Average results from the 5 tests are shown in Figure 3.15d. The tool enters the cut at around 0.6 seconds. At ~1.2 seconds, as the end mill exits the cut and the last chip breaks free, the system is subjected to a step disturbance. The response is similar to Figure 3.14a.
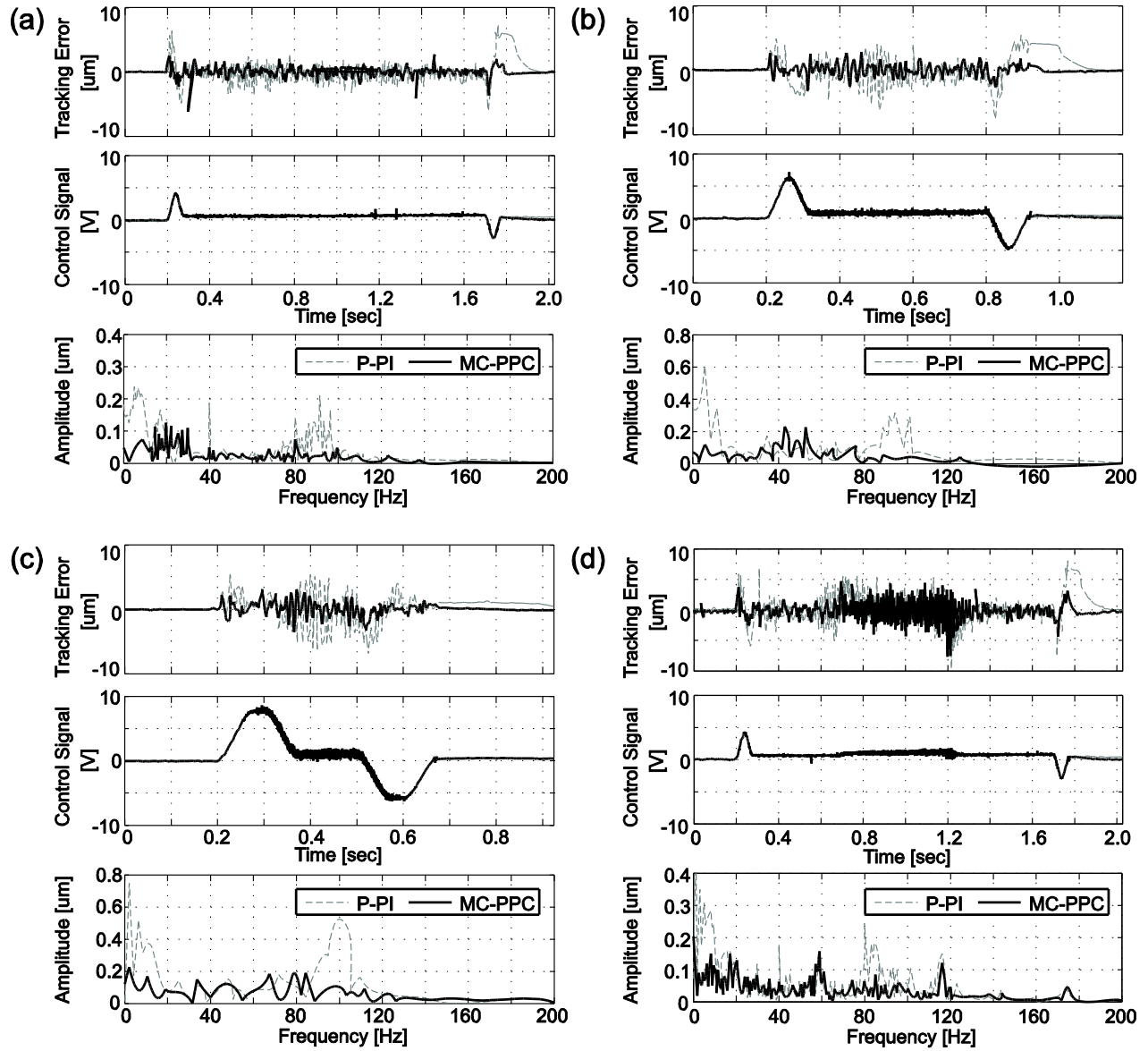
Figure 3.15: Tracking error, control signal, and FFT of tracking error for (a) 200 mm/s, (b) 500 mm/s, (c) 1000 mm/s and (d) 25.4 mm slotting at 200 mm/s in 6065 aluminum.

28

Table 3.2: Maximum and RMS errors during tracking and machining experiments

	MC-PPC		P-PI	
Velocity (mm/s)	Max. (um)	RMS (um)	Max. (um)	RMS (um)
200	3.65	0.65	7.35	1.82
500	3.34	0.84	7.47	2.24
1000	3.86	0.90	6.81	2.07
200*	7.69	1.17	9.63	2.20

*Machining experiment

3.5 Conclusions

This chapter has studied the use of the pole-placement technique to achieve active vibration damping, as well as high bandwidth disturbance rejection and position control in ball screw drives. Motivated by a simple and physically intuitive model, two of the poles are placed to speed up the damping out of axial vibrations, while the other three represent the equivalent rigid body dynamics coupled with the control law which possesses integral action. A new type of trajectory pre-filter is also presented, which is easily tuned by conducting a single tracking experiment. The pre-filter mitigates the imperfections in the drive's tracking function due to sampling, computational delay effects and the discrepancies between the actual drive response and its assumed model. The MC-PPC design and pre-filter are combined together inside the proposed scheme, which has been validated to provide superior command tracking and disturbance rejection compared to the mainstream approach of applying P-PI position-velocity cascade control. Comparison between the two schemes has been performed in frequency domain analyses, as well as step disturbance (rope snap) tests, machining and high-speed tracking experiments. The MC-PPC, on average, provides a 40-55% reduction in the maximum, and a 55-65% reduction in the RMS values of the positioning error compared to P-PI. The MC-PPC also provides a significant bandwidth improvement and dynamic stiffness increase around the 1st axial mode.

Chapter 4
Control of a Linear Motor Driven Gantry

4.1 Introduction

Direct drives provide substantial improvement in the dynamic response and accuracy over conventional ball screw drives [28], while the gantry configuration gives the potential for an extended work area while preserving a certain level of positioning accuracy. However, due to the absence of gearing between the motor and load, the drives are subjected directly to disturbance forces and any variations in the inertia, due to changes in the machine configuration or workpiece mass. Also, the gantry configuration typically results in at least one of the axes being actuated by two parallel drives where crosstalk is inevitable. This presents a significant challenge in synchronizing the axes while achieving high control bandwidth and ensuring stability. One mainstream solution is to tune the two actuators to yield an identical dynamic response, preventing one motor from falling behind the other during trajectory tracking. Although this is simpler and more reliable than master-slave type interlocking [13], it has limitations, particularly when there is strong dynamic coupling through vibration modes between the two actuators.

In feed drive control, the objective is to realize a high bandwidth in order to obtain the most favorable command following and disturbance rejection properties [29]. The control bandwidth can be significantly limited by the structural dynamics of the drive and machine tool. Recently, a new generation of controllers that actively compensate for structural dynamics using linear motors or ball screw drives has been developed, as reported in [2][19][31][34]. These controllers enhance both dynamic stiffness as well as positioning accuracy.

Applying similar techniques to gantry type motion stages presents a greater challenge due to the increased complexity of having to consider the dynamic interactions between the different actuators. Direct drive motors are well suited for applying active vibration damping due to their short response time. However, they are also more susceptible to the dynamic coupling problem encountered in gantry stages.

In literature, Teo et al. [35] have developed a dynamic model for an H-type gantry, considering only rigid body dynamics and no vibration modes or stiffness values. They have reported successful experimental results on a ball screw driven gantry using adaptive control.

Weng et al. [40] have presented the concept of sensor and actuator averaging and shown its effectiveness in controlling flexible structures, such as beams and plates. One of the main advantages of this approach is the attenuation of structural resonances without detrimentally affecting the loop phase, which would normally be associated with the use of notch filters. In this paper, the sensor/actuator averaging has been adopted in a novel controller design for a T-type gantry. The gantry was developed and built at the University of Waterloo as a new x-y stage concept for precision and micro/meso machine tools. The stage uses a single guideway, which is particularly appealing as a simple design. A secondary linear motor at the unconstrained end of the gantry beam is used to provide both stiffness and damping enhancement. The control law has been designed to take into account the dynamic coupling between the actuators and to actively attenuate the first vibration mode encountered at 94 Hz on the gantry. The stability and robustness of the design is achieved through the use of multivariable frequency domain analyses.

4.2 Experimental Setup

The experimental setup, shown in Figure 4.1 and Figure 4.2, has a T-type gantry and worktable configuration. Motion in the y-axis is provided by the gantry, while the worktable moves along the gantry in the x-axis. The worktable is supported on a precision granite surface using a 12"x12" (305 mm x 305 mm) vacuum preloaded (VPL) air bearing. The VPL uses positive and negative pressure to preload the table against the granite surface. The VPL provides both pitch moment and vertical stiffness, transmitting worktable and workpiece loads directly to the granite, rather than the gantry beam. The worktable is supported and aligned to the gantry beam using four rectangular air bearings. The y-axis is driven by two linear motors and feedback is available on both the left (primary) and right (secondary) actuators via sinusoidal encoders with 4 um signal period. The design utilizes only a single granite guideway along the y-axis, which simplifies the alignment and assembly of the stage. The gantry is constrained to the guideway by four preloaded air bearings. The secondary linear motor provides stiffness enhancement and active attenuation of yaw vibrations. The x-axis motion is generated by a third linear motor attached to the gantry beam, with feedback provided by an encoder similar to those on the y-axis.
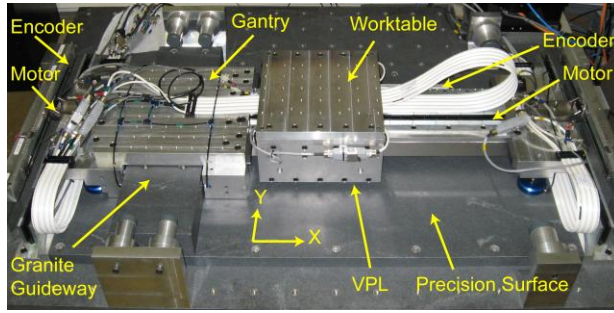
Figure 4.1: Linear motor driven T-type gantry.
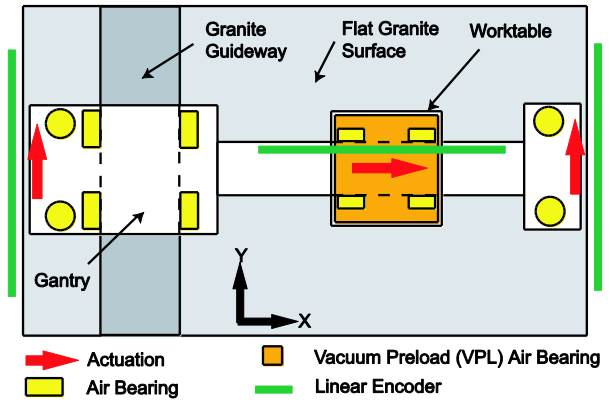
Figure 4.2: Schematic of the experimental setup.

4.3 Modeling and Identification

4.3.1 X-Axis Modeling and Identification

During identification tests, the x-axis was observed to be reasonably independent of the gantry excitation. When excitation was provided by the x-axis linear motor, the open loop acceleration frequency response function (FRF), shown in Figure 4.3, was noted to be quite flat up to 150 Hz. As a result, the x-axis position response has been modeled as a double-integrator $(x = 1/(m_x s^2))$. Considering the low frequency portion of the FRF, the control signal equivalent mass was estimated to be $m_x = 0.6977$ V/(m/s^2). Due to the use of air bearings, viscous and Coulomb friction were not observed.
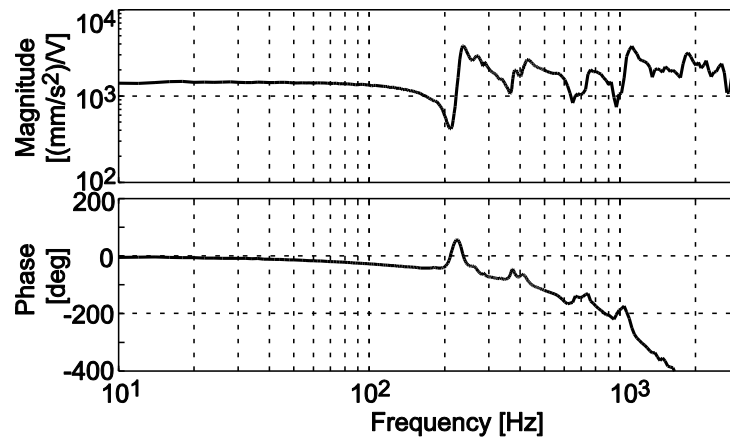
Figure 4.3: Open-loop acceleration FRF for x-axis.

4.3.2 Y-Axis Modeling

The y-axis was observed to show strong coupling between the left and right hand actuation points, in particular due to yaw vibrations that originate from the rigid body rotation of the gantry assembly around the z-axis, constrained by the torsional spring-like effect of four air bearings preloaded against each other about the y-axis granite guideway. This has been illustrated in Figure 4.4 with a simplified dynamic model.
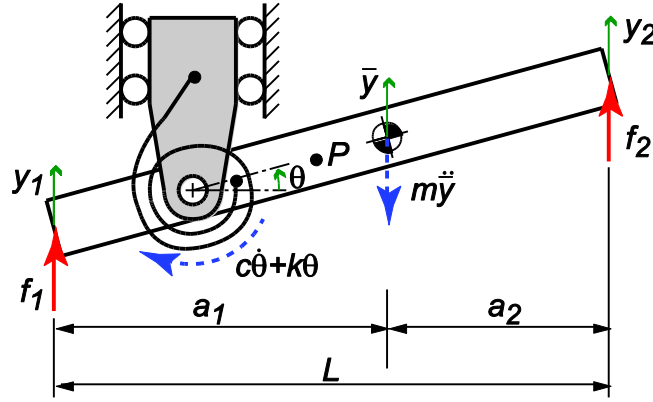
Figure 4.4: Y-axis dynamic model.

The simplified dynamic model in Figure 4.4 adequately captures the inertial characteristics and yaw motion of the gantry. By applying D'Alembert's Principle, the equations of motion can be written considering the y-axis position ($\bar{y}$) for the Center of Mass (CoM) of the beam, and the rotation angle (θ):

$$\underbrace{\begin{bmatrix} m & 0 \\ 0 & J \end{bmatrix}}_{\mathbf{M}_q} \begin{bmatrix} \ddot{\bar{y}} \\ \ddot{\theta} \end{bmatrix} + \underbrace{\begin{bmatrix} 0 & 0 \\ 0 & c \end{bmatrix}}_{\mathbf{C}_q} \begin{bmatrix} \dot{\bar{y}} \\ \dot{\theta} \end{bmatrix} + \underbrace{\begin{bmatrix} 0 & 0 \\ 0 & k \end{bmatrix}}_{\mathbf{K}_q} \begin{bmatrix} \bar{y} \\ \theta \end{bmatrix} = \underbrace{\begin{bmatrix} 1 & 1 \\ -a_1 & a_2 \end{bmatrix} \begin{bmatrix} f_1(t) \\ f_2(t) \end{bmatrix}}_{\mathbf{F}_q} \tag{4.1}$$

Above, m is the mass of the gantry assembly (including the table) and J is its moment of inertia about its center of mass. c and k are the angular damping and stiffness coefficients, respectively, provided by the air bearing assembly. a_1 and a_2 are the distance from the CoM to the left and right end points. f_1 and f_2 are the actuation forces provided by the left and right hand linear motors. Defining the kinematic transformation from $[\bar{y} \ \theta]^T$ to the displacements $[y_1 \ y_2]^T$, measured by the encoders on the left and right hand sides of the gantry:

$$\begin{bmatrix} y_1 \\ y_2 \end{bmatrix} = \mathbf{T}\begin{bmatrix} \bar{y} \\ \theta \end{bmatrix} \ , \quad \mathbf{T} = \begin{bmatrix} 1 & -a_1 \\ 1 & a_2 \end{bmatrix} \tag{4.2}$$

Equation (4.1) can be re-written in terms of $[y_1 \ y_2]^T$ as:

$$\left.\begin{aligned} &\underbrace{\begin{bmatrix} m_{11} & m_{12} \\ m_{21} & m_{22} \end{bmatrix}}_{\mathbf{M}_y=\mathbf{F}_q^{-1}\mathbf{M}_q\mathbf{T}^{-1}}\begin{bmatrix} \ddot{y}_1 \\ \ddot{y}_2 \end{bmatrix} + \underbrace{\begin{bmatrix} c_y & -c_y \\ -c_y & c_y \end{bmatrix}}_{\mathbf{C}_y=\mathbf{F}_q^{-1}\mathbf{C}_q\mathbf{T}^{-1}}\begin{bmatrix} \dot{y}_1 \\ \dot{y}_2 \end{bmatrix} + \underbrace{\begin{bmatrix} k_y & -k_y \\ -k_y & k_y \end{bmatrix}}_{\mathbf{K}_y=\mathbf{F}_q^{-1}\mathbf{K}_q\mathbf{T}^{-1}}\begin{bmatrix} y_1 \\ y_2 \end{bmatrix} = \begin{bmatrix} f_1(t) \\ f_2(t) \end{bmatrix} \\ &\text{where :} \ \ \mathbf{M}_y = \frac{1}{L^2}\begin{bmatrix} a_2^2 m + J & a_1 a_2 m - J \\ a_2 a_1 m - J & a_1^2 m + J \end{bmatrix} \ , \quad c_y = \frac{c}{L^2} \ , \quad k_y = \frac{k}{L^2} \end{aligned}\right\} \tag{4.3}$$

$L=1484$ mm is the span between the left and right motors. Using Equation (4.1), $\bar{y}(s)$ and $\theta(s)$ can also be expressed in the Laplace domain in terms of $f_1(s)$ and $f_2(s)$. Following this, and applying the coordinate transformation in Equation (4.2), the following transfer matrix relationships between the input forces $[f_1 \ f_2]^T$ and measured endpoint displacements $\boldsymbol{y} = [y_1 \ y_2]^T$ can be obtained:

$$\begin{bmatrix} y_1 \\ y_2 \end{bmatrix} = \begin{bmatrix} G_{11} & G_{12} \\ G_{21} & G_{22} \end{bmatrix}\begin{bmatrix} f_1 \\ f_2 \end{bmatrix}, \quad \begin{aligned} G_{11} &= \frac{1}{ms^2} + \frac{a_1^2}{Js^2 + cs + k} & G_{12} &= \frac{1}{ms^2} - \frac{a_1 a_2}{Js^2 + cs + k} \\ G_{21} &= \frac{1}{ms^2} - \frac{a_2 a_1}{Js^2 + cs + k} & G_{22} &= \frac{1}{ms^2} + \frac{a_2^2}{Js^2 + cs + k} \end{aligned} \tag{4.4}$$

4.3.3 Y-Axis Identification

The parameters for the y-axis model in Equation (4.3) have been identified by applying Least Squares fitting on the frequency response data, following a methodology similar to the one in [27]. Here, additional equality constraints have also been incorporated for the total mass and viscous friction, which were estimated ahead of time. The equations of motion in Equation (4.3) can be written in the frequency domain as:

$$\begin{bmatrix} m_{11} & m_{12} \\ m_{12} & m_{22} \end{bmatrix}(j\omega)^2\begin{bmatrix} y_1 \\ y_2 \end{bmatrix} + \begin{bmatrix} c_{11} & c_{12} \\ c_{12} & c_{22} \end{bmatrix}(j\omega)\begin{bmatrix} y_1 \\ y_2 \end{bmatrix} + \begin{bmatrix} k_{11} & k_{12} \\ k_{12} & k_{22} \end{bmatrix}\begin{bmatrix} y_1 \\ y_2 \end{bmatrix} = \begin{bmatrix} u_1 \\ u_2 \end{bmatrix} \tag{4.5}$$

which can be rearranged as,

$$
\underbrace{\begin{bmatrix} k_{11} - \omega^2 m_{11} + j\omega c_{11} & k_{12} - \omega^2 m_{12} + j\omega c_{12} \\ k_{12} - \omega^2 m_{12} + j\omega c_{12} & k_{22} - \omega^2 m_{22} + j\omega c_{22} \end{bmatrix}}_{\hat{\mathbf{G}}^{-1}} \underbrace{\begin{bmatrix} y_1(\omega) \\ y_2(\omega) \end{bmatrix}}_{\mathbf{y}} = \underbrace{\begin{bmatrix} u_1(\omega) \\ u_2(\omega) \end{bmatrix}}_{\mathbf{u}}
\tag{4.6}
$$

The simplified model assumes that the MIMO plant $\mathbf{G}$ contains only one mode. Assuming that the estimated model $\hat{\mathbf{G}}$ closely approximates the real plant $(\hat{\mathbf{G}} \approx \mathbf{G})$ in a particular frequency range of interest which includes only this mode,

$$
\mathbf{G}(\omega)\hat{\mathbf{G}}^{-1} \cong \mathbf{I}, \text{ where } \mathbf{G}(\omega) = \begin{bmatrix} g_{11}(\omega) + jh_{11}(\omega) & g_{12}(\omega) + jh_{12}(\omega) \\ g_{21}(\omega) + jh_{21}(\omega) & g_{22}(\omega) + jh_{22}(\omega) \end{bmatrix}
\tag{4.7}
$$

Above, g and h represent the measured real and imaginary components of G_{11}, G_{12}, G_{21}, and G_{22}. By separating the real and imaginary response terms from the dynamic system parameters, Equation (4.7) can be rewritten in parameter-regressor form $(\mathbf{Y} = \Phi\Theta)$ by defining the parameter vector, Θ :

$$
\Theta = \begin{bmatrix} m_{11} & m_{12} & m_{22} & c_{11} & c_{12} & c_{22} & k_{11} & k_{12} & k_{22} \end{bmatrix}^T
\tag{4.8}
$$

and regressor matrix, $\phi(\omega)$, at a particular frequency ω,

$$
\phi(\omega) = \begin{bmatrix}
-\omega^2 g_{11}(\omega) & -\omega^2 g_{12}(\omega) & 0 & -\omega^2 h_{11}(\omega) & -\omega^2 h_{12}(\omega) & 0 & g_{11}(\omega) & g_{12}(\omega) & 0 \\
-\omega^2 h_{11}(\omega) & -\omega^2 h_{12}(\omega) & 0 & \omega g_{11}(\omega) & \omega g_{12}(\omega) & 0 & h_{11}(\omega) & h_{12}(\omega) & 0 \\
0 & -\omega^2 g_{11}(\omega) & -\omega^2 g_{12}(\omega) & 0 & -\omega h_{11}(\omega) & -\omega h_{12}(\omega) & 0 & g_{11}(\omega) & g_{12}(\omega) \\
0 & -\omega^2 h_{11}(\omega) & -\omega^2 h_{12}(\omega) & 0 & \omega g_{11}(\omega) & \omega g_{12}(\omega) & 0 & h_{11}(\omega) & h_{12}(\omega) \\
-\omega^2 g_{21}(\omega) & -\omega^2 g_{22}(\omega) & 0 & -\omega h_{21}(\omega) & -\omega h_{22}(\omega) & 0 & g_{21}(\omega) & g_{22}(\omega) & 0 \\
-\omega^2 h_{21}(\omega) & -\omega^2 h_{22}(\omega) & 0 & \omega g_{21}(\omega) & \omega g_{22}(\omega) & 0 & h_{21}(\omega) & h_{22}(\omega) & 0 \\
0 & -\omega^2 g_{21}(\omega) & -\omega^2 g_{22}(\omega) & 0 & -\omega h_{21}(\omega) & -\omega h_{22}(\omega) & 0 & g_{21}(\omega) & g_{22}(\omega) \\
0 & -\omega^2 h_{21}(\omega) & -\omega^2 h_{22}(\omega) & 0 & \omega g_{21}(\omega) & \omega g_{22}(\omega) & 0 & h_{21}(\omega) & h_{22}(\omega)
\end{bmatrix}
\tag{4.9}
$$

Given the FRF measurements at a set of frequencies, $\omega_1, \omega_{2,...}, \omega_N$, around the mode of interest $(\omega_1 = 60\,\text{Hz}, \omega_N = 150\,\text{Hz})$, we obtain,

$$
\begin{bmatrix} y(\omega_1) \\ y(\omega_2) \\ \vdots \\ y(\omega_N) \end{bmatrix}_{8N\times 1} = \underbrace{\begin{bmatrix} \phi_1 \\ \phi_2 \\ \vdots \\ \phi_N \end{bmatrix}}_{\Phi}{}_{8N\times 9} \cdot \Theta + \begin{bmatrix} e_1 \\ e_2 \\ \vdots \\ e_N \end{bmatrix}_{8N\times 1}
$$

$\underbrace{}_{Y}$

(4.10)

The objective is to find Θ that minimizes,

$$
J = (\mathbf{Y} - \Phi\Theta)^T \mathbf{W}(\mathbf{Y} - \Phi\Theta)
$$

(4.11)

Above, $\mathbf{W}$ is a weighting matrix which allows the importance of the measurement at each frequency to be specified. The weighting matrix has the following form:

$$
\mathbf{W}_{8N\times 8N} = \begin{bmatrix} \mathbf{w}_1 & 0 & \cdots & 0 \\ 0 & \mathbf{w}_2 & \cdots & 0 \\ \vdots & \vdots & \ddots & \vdots \\ 0 & 0 & \cdots & \mathbf{w}_N \end{bmatrix}, \mathbf{w}_j = w_j \mathbf{I}_{8\times 8}
$$

(4.12)

In our estimation, all measurements for the frequency range of interest (60-150 Hz) were weighted equally ($w_j = 1$).

The total control signal equivalent mass ($m_y = 2.722$ V/(m/s^2)) and its distribution on the left ($\alpha_1 = m_1/m_y$) and right hand ($\alpha_2 = m_2/m_y$) sides of the gantry were estimated by correlating the control signal (i.e., force demand) during controlled tracking tests with the commanded acceleration profile using Least Squares. The variation of the mass distribution with x-axis position is shown in Figure 4.5.
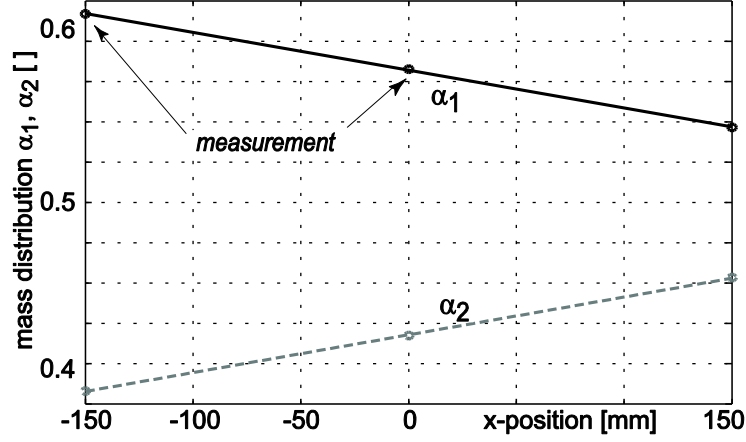
Figure 4.5: Mass distribution variation with x-axis location.

The known mass distribution $(m_1 = m_{11} + m_{21};\ m_2 = m_{12} + m_{22})$ identified during these controlled tracking experiments, a zero external viscous friction condition $(c_{11} - 2c_{12} + c_{22} = 0)$, and symmetric stiffness $(k_{11} = -k_{12} = k_{22})$ and damping $(c_{11} = -c_{12} = c_{22})$ have been incorporated into the estimation as constraints using Lagrange multipliers. The constraints are stacked together in matrix form as $\mathbf{L}\Theta = \xi$,

$$\underbrace{\begin{bmatrix} 1 & 1 & 0 & & & & & \\ 0 & 1 & 1 & & \mathbf{0}_{2\times3} & & \mathbf{0}_{2\times3} & \\ & \mathbf{0}_{1\times3} & & 1 & 2 & 1 & \mathbf{0}_{1\times3} & \\ & & & 1 & 0 & -1 & & \\ & \mathbf{0}_{2\times3} & & 1 & 1 & 0 & \mathbf{0}_{2\times3} & \\ & & & & & & 1 & 0 & -1 \\ & \mathbf{0}_{2\times3} & & & \mathbf{0}_{2\times3} & & 1 & 1 & 0 \end{bmatrix}}_{\mathbf{L}} \underbrace{\begin{bmatrix} m_{11} \\ m_{12} \\ m_{22} \\ c_{11} \\ c_{12} \\ c_{22} \\ k_{11} \\ k_{12} \\ k_{22} \end{bmatrix}}_{\Theta} = \underbrace{\begin{bmatrix} m_1 \\ m_2 \\ 0 \\ 0 \\ 0 \\ 0 \\ 0 \\ 0 \\ 0 \end{bmatrix}}_{\xi} \tag{4.13}$$

The objective function including the constraints is:

$$J' = (\mathbf{Y} - \Phi\Theta)^T \mathbf{W}(\mathbf{Y} - \Phi\Theta) + \Lambda^T (\mathbf{L}\Theta - \xi) \tag{4.14}$$

37

By setting gradients with respect to the parameters and the Lagrange multipliers (Λ) equal to zero ($\partial J'/\partial \Theta = 0$ and $\partial J'/\partial \Lambda = 0$), the least squares solution for $[\Theta \quad \Lambda]^T$ can be obtained as,

$$\underbrace{\begin{bmatrix} 2\Phi^T\mathbf{W}\Phi & \mathbf{L}^T \\ \mathbf{L} & \mathbf{0} \end{bmatrix}}_{\mathbf{A}} \begin{bmatrix} \Theta \\ \Lambda \end{bmatrix} = \underbrace{\begin{bmatrix} 2\Phi^T\mathbf{W}\mathbf{Y} \\ \xi \end{bmatrix}}_{\mathbf{b}} \Rightarrow \begin{bmatrix} \Theta \\ \Lambda \end{bmatrix} = \mathbf{A}^{-1}\mathbf{b} \tag{4.15}$$

This gives the parameters Θ, which allows the control signal equivalent inertia ($J = J_0 + m_x(d + x)^2$), torsional damping (c) and stiffness (k) to be calculated using the relations in Equation (4.3). The identified parameters are,

$$\begin{aligned} &J = J_0 + m_x(d+x)^2, \text{ where } J_0 = 0.4342\,[\text{Vms}^2], d = 0.1655\,[\text{m}], \\ &m_x = 0.6977\,[\text{V/(m/s}^2)]; c = 18.17\,[\text{Vms}]; k = 159.2\times10^3\,[\text{Vm}] \end{aligned} \tag{4.16}$$

In FRF measurements, shown in Figure 4.6, the lowest resonance due to yaw vibrations was noted at 94 Hz. The vibration mode registered at 382 Hz is attributed to the bending of the gantry beam about the z-axis. The mode at 320 Hz could not be attributed to either pitching or bending of the gantry, and requires more investigation. As the x-axis location of the table varies, the inertia distribution on the left and right hand sides will also change. As a result, the vibration modes were observed to shift in frequency by less than $\pm 6\%$.
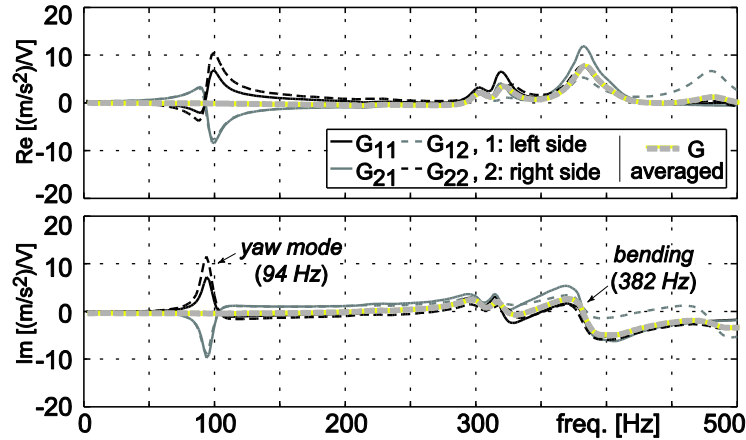
Figure 4.6: Y-axis acceleration response.

The model in Equations (4.1) and (4.16) predicts the dependency of the rotational inertia, hence the yaw mode, on the x-axis position of the table. At $x = 0$ mm, the first mode is predicted to be at 94.3 Hz with 3.4% damping. The model for the table at different positions has been shown in Figure 4.7, and is in good agreement with the experimental FRFs.
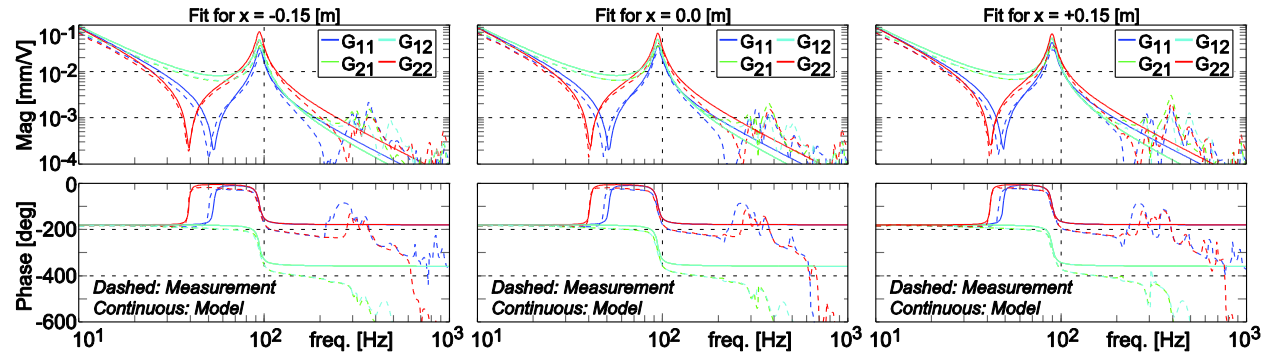
Figure 4.7: Model identified for y-axis position FRF with table at x = -0.15 m (left), x = 0.0 m (center) and x = +0.15 m (right)

Certain structural modes were also confirmed using impact hammer testing, with feedback from the linear encoders. The hammer test results are shown in Figure 4.8.
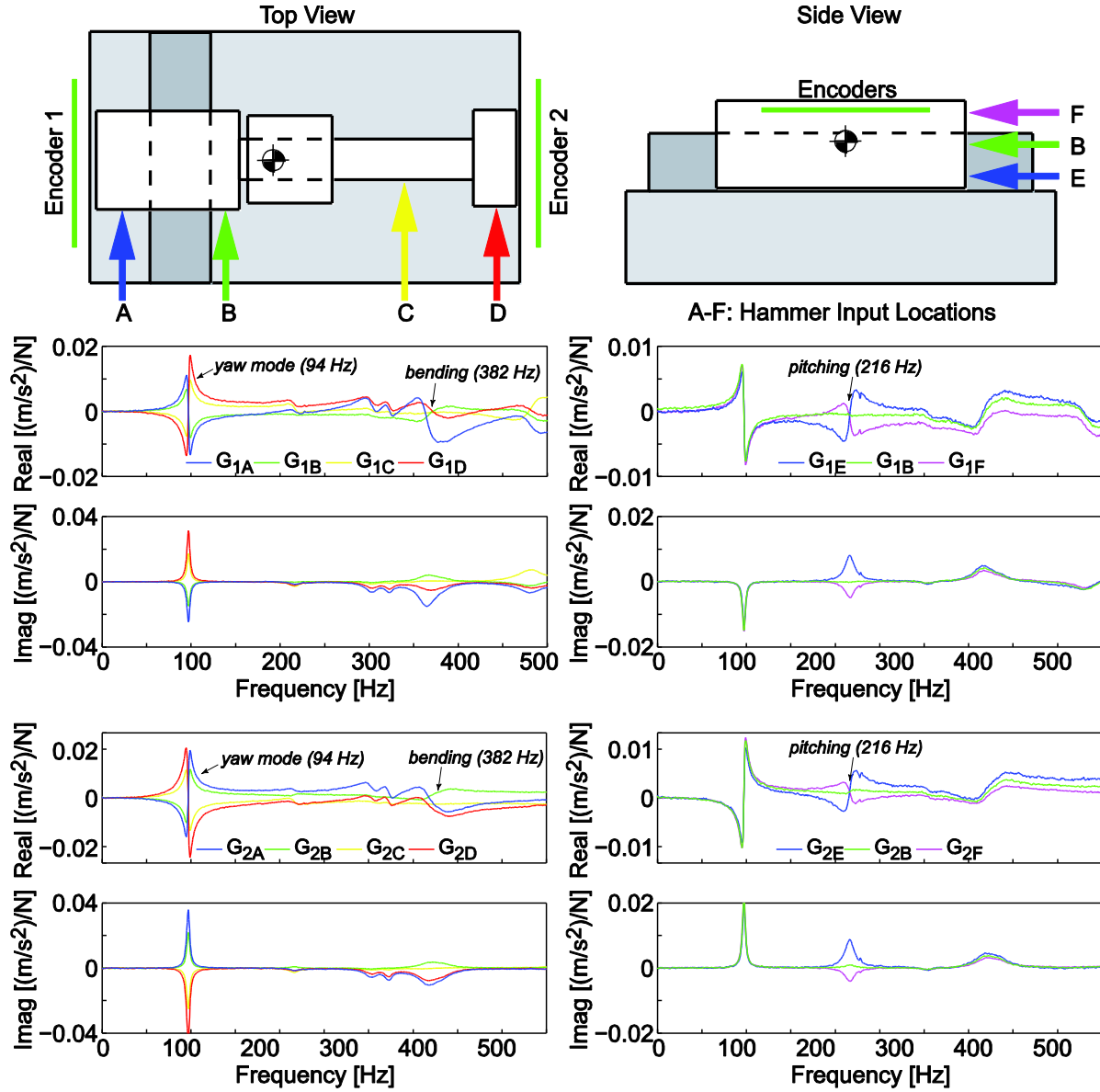
Figure 4.8: Impact hammer test results.

By varying the hammer input location along the length of the gantry, the shape of the yaw and bending modes can be seen. At 94 Hz, the excitation points on the same side of the CoM are moving in phase, and are 180 degrees out of phase with points on the opposite side. The magnitude of the resonance at each point is proportional to the distance from the CoM. This indicates a rigid-body rotation about the center of mass. At 382 Hz, points A and D are moving in phase, while B is out of phase. Point C appears to be close to a node of this mode. This is attributed to the first bending mode of the beam.

40

Also, by moving the excitation input from the bottom to the top of the gantry, an additional mode at 216 Hz can be observed. The top and bottom of the gantry are moving out of phase, indicating that the gantry is pitching about the x-axis. The excitation point B is close to the neutral point of this mode, which is assumed to be the gantry CoM. Similarly, the pitching mode is not observed in the FRF's when excitation is provided by the motors, since the motors were vertically positioned to apply their actuation force very close to the CoM.

Overall, the y-axis modeling and identification results indicate that the most significant obstacle to achieving high control performance is the yaw vibration mode at 94 Hz. This mode dramatically limited the control bandwidth to around 16 Hz when stabilization was attempted using independent PID controllers for both actuators. Therefore, this mode has been analyzed and taken into account in the controller design, in order to further improve the y-axis performance, in the proceeding sections.

4.4 Controller Design

4.4.1 X-Axis Controller Design

The x-axis controller was designed using classical loop shaping methodology [11]. First, a desired crossover frequency (ω_c) and phase margin (PM) are chosen. The highest crossover that could be achieved while maintaining adequate stability margins was $\omega_c = 130$ Hz. The phase margin was chosen to be 35°. In order to eliminate steady-state errors, integral action was also added. The integral term takes the form $(T_i s + 1)/s$. T_i is designed to give a phase lag of $\phi_{PI} = -10°$ at the crossover frequency. To stabilize the x-axis, the required phase lead at ω_c is found as,

$$\phi_{lead} = -180° + PM - \angle G_x(j\omega_c) - \phi_{PI} = 126°$$

(4.17)

Above, $\angle G_x(j\omega_c)$ is the phase angle of the x-axis position FRF at ω_c. Since the required lead cannot be provided by a single lead filter (>90°) or a derivative term, two lead filters are used, each of which generates +63° phase shift at ω_c. This requires each filter to have a lead ratio of $\gamma = \sqrt{(1 + \sin 63°)/(1 - \sin 63°)} = 4.2$ [11]. The filter pole is placed at $a = \gamma\omega_c$ and the zero at $1/T_d = \omega_c/\gamma$. The gain K is adjusted to make the loop magnitude unity at ω_c. Hence, the double lead and integral compensator becomes:

41

$$C(s) = K \frac{(T_i s + 1)}{s} \cdot \frac{(T_d s + 1)^2}{(s/a + 1)^2} \tag{4.18}$$

The loop transfer function, $L(j\omega) = G(j\omega)C(j\omega)$, and the Nyquist plot are used to inspect the crossover frequency and phase margin. The magnitude of the sensitivity function, $S(j\omega) = 1/(1 + L(j\omega))$ is the inverse of the distance from the Nyquist plot to the critical "-1" point, and so can also be used as a measure of stability [32]. A *1*st order low pass at 1200 Hz, and Notch filters in the form $N(s) = (s^2 + 2\zeta_N \omega_N s + \omega_N^2)/(s^2 + 2\zeta_D \omega_D s + \omega_D^2)$ at 186 Hz (ζ_N =0.6, ζ_D=0.7), 332 Hz (ζ_N =0.3, ζ_D=0.7), and 404 Hz (ζ_N =0.2, ζ_D=0.7), were inserted to attenuate high frequency modes and mitigate undesirable peaks in $|S(j\omega)|$. When the design was complete, the specifications for ω_c and *PM* were achieved. The controller is active where $|S| < 1.0$, which indicates an improvement over the open-loop disturbance response. This range was up to 98 Hz. The continuous-time controller has been discretized using pole-zero matching with a sampling frequency of $T_s = 15$ kHz. The corresponding loop magnitude, Nyquist and sensitivity plots are shown in Figure 4.9.
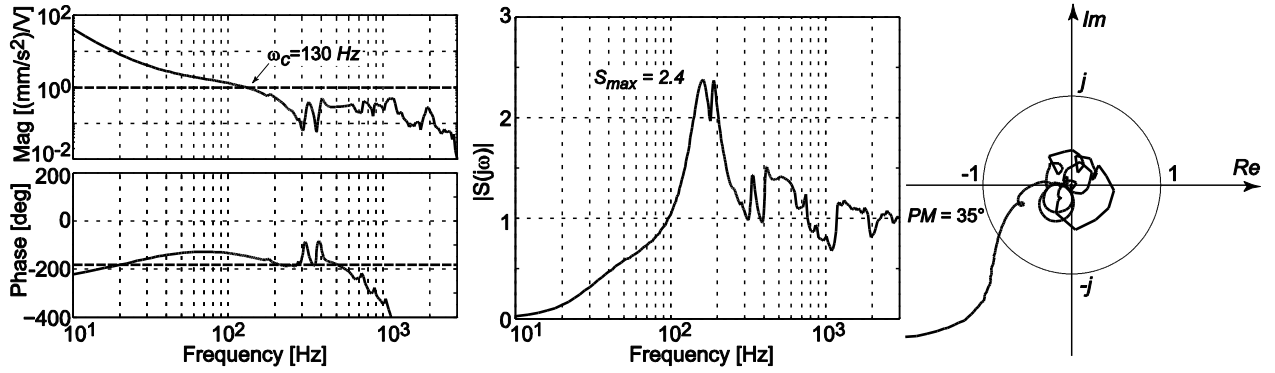
Figure 4.9: X-axis loop gain (left), sensitivity (center) and Nyquist plot (right).

Feedforward inertia compensation and a trajectory pre-filter were added to further improve command tracking. The control effort for inertia compensation is,

$$u_{ff} = m_x \ddot{x}_r \tag{4.19}$$

42

An additional trajectory pre-filter was designed to remove any remaining correlations of the velocity, acceleration, jerk, and snap (4th derivative) commands from the tracking error, by offsetting the position commands accordingly:

$$x_r' = x_r + K_{vel}\dot{x}_{rf} + K_{acc}\ddot{x}_{rf} + K_{jerk}\dddot{x}_{rf} + K_{snap}x_{rf}^{(IV)}$$

where

$$\dot{x}_{rf}(s) = G_{lpf}^{\ 2}(s) \cdot \dot{x}(s)$$
$$\ddot{x}_{rf}(s) = G_{lpf}^{\ 3}(s) \cdot \ddot{x}(s)$$
$$\dddot{x}_{rf}(s) = G_{lpf}^{\ 4}(s) \cdot \dddot{x}(s)$$
$$x_{rf}^{(IV)}(s) = G_{lpf}^{\ 5}(s) \cdot x^{(IV)}(s)$$

(4.20)

are low-pass filtered versions of the commanded velocity, acceleration, jerk and snap. The low-pass filter was designed in the form $G_{lpf}(s) = \omega_c/(s + \omega_c)$, where $\omega_c = 80\,\mathrm{Hz}$. The pre-filter gains were identified using Least Squares from the results of a single tracking experiment.

4.4.2 Y-Axis Controller Design

Due to the strong dynamic coupling between the left and right hand actuators, particularly through yaw vibrations at 94 Hz, design of the y-axis controller proved to be more challenging. The overall scheme is shown in Figure 4.10. The principal regulation function is achieved by controlling the CoM motion for the gantry, by using sensor and actuator averaging and loop shaping. Active vibration damping is added to improve the dynamic stiffness against external disturbances, such as machining forces. Actuator level integral action is also added to eliminate steady-state positioning errors at the servo level. To enhance the command tracking, feedforward inertia compensation and a trajectory pre-filter are included into the scheme. Furthermore, a filter pack comprising of notch and low-pass filters ensures that unwanted sensitivity peaks, which may lead to poor robustness or instability, are avoided in the feedback loop.
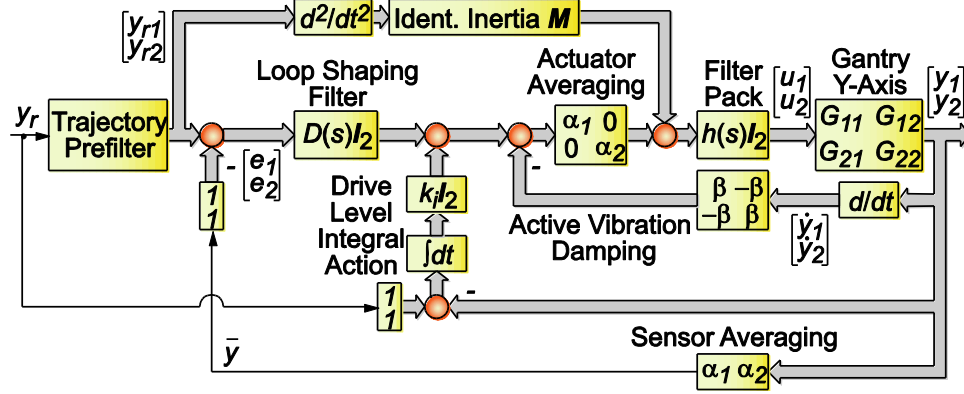
43

Figure 4.10: Y-Axis (gantry) control scheme.

In the following sections, the function and design of each of the components will be explained. One of the most crucial issues with the MIMO controller is guaranteeing stability with adequate margins. For this purpose, frequency domain analyses were conducted during the design iterations, using several concepts from multivariable control:

Singular Value Decomposition (SVD)

Singular value decomposition (SVD) is a useful matrix factorization which allows several SISO control concepts to be intuitively extended to MIMO systems. The SVD theorem states that any matrix, $\mathbf{A}_{n \times m}$, can be decomposed into a product of three matrices:

$$\mathbf{A}_{n \times m} = \mathbf{U}_{n \times n} \Sigma_{n \times m} \mathbf{V}_{m \times m}^{H} \tag{4.21}$$

where $\mathbf{V}$ and $\mathbf{U}$ are orthogonal rotation matrices which specify the input and output directions, respectively. $\Sigma = diag\{\sigma_1, \ldots, \sigma_n\}$ is a unique scaling matrix containing the singular values, σ_i, of $\mathbf{A}$, in descending order. The maximum singular value of $\mathbf{A}$ is denoted as $\overline{\sigma}\{\mathbf{A}\} = \sigma_1$ and gives the largest matrix gain for any input direction. Likewise, the minimum singular value is $\underline{\sigma}\{\mathbf{A}\} = \sigma_n$ and corresponds to the smallest matrix gain for any input direction.

Loop Transfer Matrix

Considering the experimentally measured open loop position frequency response matrix $\mathbf{G}(j\omega)$, and the feedback controller response $\mathbf{K}(j\omega)$ (which here can be computed analytically from Equation (4.30)), the multivariable loop transfer function matrix is defined as $L(j\omega) = \mathbf{G}(j\omega)\mathbf{K}(j\omega)$. $\mathbf{L}(j\omega)$ shows the

combined amplification of the controller and plant. In particular, the feedback is active where $\overline{\sigma}\{\mathbf{L}(j\omega)\} > 1$.

MIMO Nyquist Criterion

According to the MIMO Nyquist Stability Criterion, stability is guaranteed when the locus of $\det\{\mathbf{I} + \mathbf{L}(j\omega)\}$ makes no counter-clockwise encirclement of the origin in the complex plane and does not pass through the origin [32].

MIMO Sensitivity Function

The MIMO sensitivity function is defined as $\mathbf{S}(j\omega) = (\mathbf{I} + \mathbf{L}(j\omega))^{-1}$. $M_S = \max_{\omega} \overline{\sigma}(\mathbf{S}(j\omega)) = \|S\|_{\infty}$ is an important indicator of stability margin, which in practice should not be much larger than $M_S = 1.5 - 2.5$. It is also noted that for frequencies where $\overline{\sigma}(\mathbf{S}(j\omega)) < 1$, the controller is actively rejecting disturbances in all input directions.

Disturbance Transfer Matrix

The disturbance transfer matrix is analyzed to determine the disturbance rejection capability of the system. For the open loop case with our gantry model, it is equal to the MIMO plant, $\mathbf{G}(j\omega)$. When feedback is added, it becomes $(\mathbf{I} + \mathbf{L}(j\omega))^{-1}\mathbf{G}(j\omega) = \mathbf{S}(j\omega)\mathbf{G}(j\omega)$. In particular, the upper singular value of the disturbance transfer matrix is examined, as it indicates the maximum possible amplification of a disturbance acting on the gantry drive system.

Considering that a_1 and a_2 locate the CoM from the left and right actuation points, the mass distribution for the two sides of the gantry can be expressed as:

$$\alpha_1 = m_1 / m = a_2 / L \ , \ \ \alpha_2 = m_2 / m = a_1 / L \ , \ \ \text{where:} \ a_1 + a_2 = L \tag{4.22}$$

When the left and right encoder readings are averaged proportionally to their mass ratios (sensor averaging), the CoM displacement can be computed as:

$$\begin{bmatrix} \bar{y} \\ \theta \end{bmatrix} = \mathbf{T}^{-1} \begin{bmatrix} y_1 \\ y_2 \end{bmatrix} = \begin{bmatrix} a_2/L & a_1/L \\ -1/L & 1/L \end{bmatrix} \begin{bmatrix} y_1 \\ y_2 \end{bmatrix} \Rightarrow \bar{y} = \alpha_1 y_1 + \alpha_2 y_2 \qquad (4.23)$$

On the other hand, defining the total actuation force as $f_T = f_1 + f_2$, if the total actuation force is distributed to the left and right hand drives proportionally to the mass they actuate (i.e., $f_1 = \alpha_1 f_T$ and $f_2 = \alpha_2 f_T$), the following averaged transfer function ($\overline{G}(s)$) determines the relationship between the CoM displacement ($\bar{y}$) and total actuation force (f_T):

$$\bar{y} = \alpha_1 y_1 + \alpha_2 y_2 = \underbrace{\left[\alpha_1(G_{11}\alpha_1 + G_{12}\alpha_2) + \alpha_2(G_{21}\alpha_1 + G_{22}\alpha_2)\right]}_{\overline{G}(s)} f_T \qquad (4.24)$$

By substituting G_{11}, G_{12}, G_{21}, and G_{22} from Equation (4.4), the sensor and actuator averaged transfer function interestingly becomes $\overline{G}(s) = 1/(ms^2)$, in which the effect of the yaw mode vanishes. From a feedback control point of view, this can provide a major advantage in increasing the bandwidth while avoiding the phase distortion associated with notch filtering, similar to the idea reported in [40]. The loop shaping filter $D(s)$ is designed to control the averaged transfer function $\overline{G}(s)$ derived in Equation (4.24). The loop shaping methodology allows higher flexibility in specifying the loop magnitude and phase, compared to more mainstream design techniques, such as P-PI position-velocity cascade or PID control. The feedback controller that realizes CoM position control through sensor/actuator averaging and loop shaping can be written as:

$$\begin{bmatrix} u_{1,CoM} \\ u_{2,CoM} \end{bmatrix} = \underbrace{\begin{bmatrix} \alpha_1 & 0 \\ 0 & \alpha_2 \end{bmatrix}}_{\substack{\text{Actuator} \\ \text{Averaging}}} \begin{bmatrix} 1 \\ 1 \end{bmatrix} D(s) \underbrace{\begin{bmatrix} \alpha_1 & \alpha_2 \end{bmatrix}}_{\substack{\text{Sensor} \\ \text{Averaging}}} \begin{bmatrix} e_{1y}(s) \\ e_{2y}(s) \end{bmatrix} \quad , \quad \begin{matrix} e_{1y} = y_{1r} - y_1 \\ e_{2y} = y_{2r} - y_2 \end{matrix} \qquad (4.25)$$

The loop shaping filter, $D(s)$ is a lead filter designed to yield a 40° phase margin at the crossover corresponding to the rigid-body motion of the CoM,

$$D(s) = K \frac{T_d s + 1}{s/a + 1} \qquad (4.26)$$

In this application, this crossover frequency was chosen as $\omega_c = 60\,\text{Hz}$. The lead ratio, $\gamma = a/\omega_c = \omega_c/(1/T_d)$, must be designed iteratively based on the phase associated with the averaged transfer function, $\overline{G}(j\omega_c)$ and filter pack $h(j\omega_c)$ at the crossover frequency. The design of the filter pack is detailed later in this section.

In practical implementation, the mass distribution estimates will not be exact. In addition, cutting or other external process forces may still excite the yaw mode vibrations. Hence, as a further measure, active damping is injected into the loop by emulating the effect of a torsional damper:

$$\begin{bmatrix} u_{1,AD} \\ u_{2,AD} \end{bmatrix} = -\begin{bmatrix} \alpha_1 & 0 \\ 0 & \alpha_2 \end{bmatrix}\begin{bmatrix} \beta & -\beta \\ -\beta & \beta \end{bmatrix}s\begin{bmatrix} y_1(s) \\ y_2(s) \end{bmatrix} = \beta\begin{bmatrix} \alpha_1 s(y_2 - y_1) \\ \alpha_2 s(y_1 - y_2) \end{bmatrix} \tag{4.27}$$

Noting that $\theta = (y_2 - y_1)/L$, $\alpha_1 = a_2/L$, and $\alpha_2 = a_1/L$, by checking the characteristic equation after substituting Equation (4.27) into Equation (4.1) as $f_1 = u_{1,AD}$ and $f_2 = u_{2,AD}$, it can be seen that active vibration damping effectively increases the torsional damping coefficient by $2\beta a_1 a_2$, with each actuator contributing equally to this damping increase:

$$(Js^2 + cs + k)\theta(s) = -\underbrace{a_1 a_2 \beta s\theta}_{\substack{\text{Actuator1} \\ \text{Contribution}}} - \underbrace{a_1 a_2 \beta s\theta}_{\substack{\text{Actuator2} \\ \text{Contribution}}} \Rightarrow [Js^2 + (c + 2a_1 a_2 \beta)s + k]\theta(s) = 0 \tag{4.28}$$

Here, β was designed to provide 590% increase over the existing damping provided by the air bearing assembly. Another advantage of the active damping is that it reduces the sensitivity, $\overline{\sigma}(\mathbf{S}(j\omega))$, in the vicinity of the yaw vibration mode at 94 Hz, making it possible to achieve more aggressive controller designs with higher bandwidths. In the current design, the active damping was necessary to avoid instability, as can be seen in both the frequency domain analysis and time domain results in Figure 4.11. When active damping is disabled, the system immediately enters yaw vibrations which are two orders of magnitude larger than the errors during high speed tracking tests with active damping.
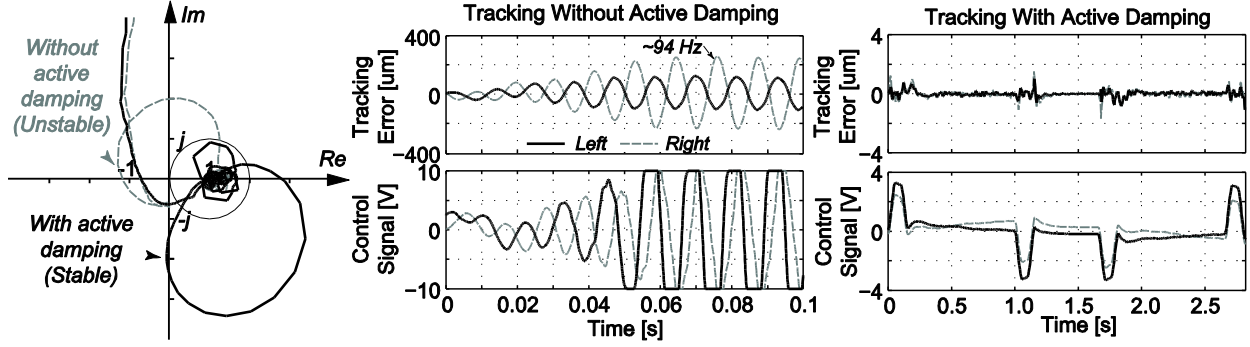
Figure 4.11: Contribution of active damping demonstrated in frequency and time domain results. Tracking results are for a 200 mm/s velocity, 2 m/s² acceleration, 50 m/s³ jerk trajectory.

By averaging the sensor data, the situation may arise where opposing servo errors at y_1 and y_2 give the false impression that the CoM error is zero (i.e., $\alpha_1 e_{1y} = -\alpha_2 e_{2y}$). Thus, integral action has been implemented at the actuator level as follows:

$$\begin{bmatrix} u_{1,i} \\ u_{2,i} \end{bmatrix} = \begin{bmatrix} \alpha_1 & 0 \\ 0 & \alpha_2 \end{bmatrix} \frac{k_i}{s} \begin{bmatrix} e_{1y}(s) \\ e_{2y}(s) \end{bmatrix} \tag{4.29}$$

Aggressive values for k_i were observed to excite low frequency machine base vibrations, which, when interacting with the control law, resulted in vibrations around 36 Hz. This problem was predicted and avoided using multivariable stability analyses conducted throughout the design, as seen in Figure 4.12.
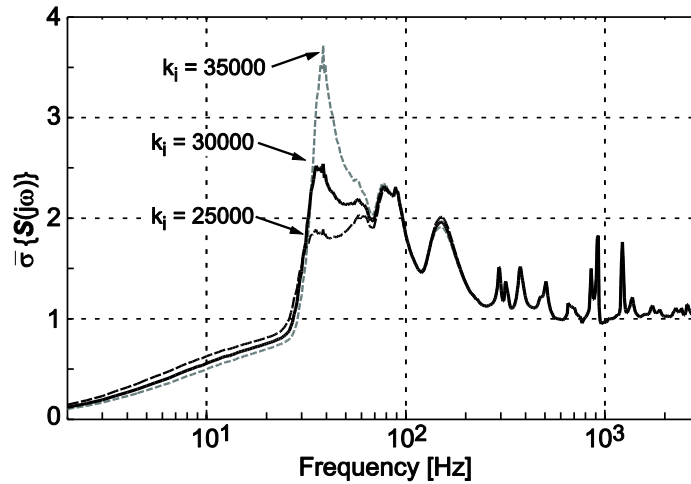
Figure 4.12: Maximum singular values of sensitivity function for various integral action gains (k_i)

Frequencies at which $\overline{\sigma}(\mathbf{S}) > 1.5\text{-}2.5$ have been attenuated by placing notch and low-pass filters. As a result, $h(s)$ was designed to contain notch filters at 110 Hz ($\zeta_N = 0.5$, $\zeta_D = 0.7$), 320 Hz ($\zeta_N = 0.2$, $\zeta_D = 0.9$), 400 Hz ($\zeta_N = 0.15$, $\zeta_D = 1.0$), and 940 Hz ($\zeta_N = 0.6$, $\zeta_D = 0.75$) and a 2nd order low-pass filter at 450 Hz. Since the active vibration damping results in a second crossover frequency around $\omega_{c,2} = 124\,\text{Hz}$, a second lead filter ($\omega_{lead} = 154\,\text{Hz}$, $\phi_{lead} = 70°$) was also inserted in the filter pack to alleviate the corresponding peak in sensitivity.

By combining the sensor and actuator averaged loop shaping, active damping, and integral action terms from Equations (4.26), (4.27), and (4.29), together with the filter pack $h(s)$, the overall feedback controller can be obtained as:

$$\mathbf{K}(s) = h(s) \begin{bmatrix} \alpha_1 & 0 \\ 0 & \alpha_2 \end{bmatrix} \left\{ \begin{bmatrix} 1 \\ 1 \end{bmatrix} D(s) \begin{bmatrix} \alpha_1 & \alpha_2 \end{bmatrix} + \begin{bmatrix} \beta & -\beta \\ -\beta & \beta \end{bmatrix} s + \frac{k_i}{s} \begin{bmatrix} 1 & 0 \\ 0 & 1 \end{bmatrix} \right\} \tag{4.30}$$

To further improve the command tracking, feedforward inertial compensation and a trajectory pre-filter were added as shown in Figure 4.10, in a similar manner to the x-axis design. The inertia compensation is in the form,

$$\begin{bmatrix} u_{ff1} \\ u_{ff2} \end{bmatrix} = \begin{bmatrix} \hat{m}_{11} & \hat{m}_{12} \\ \hat{m}_{12} & \hat{m}_{22} \end{bmatrix} \begin{bmatrix} \ddot{y}_{r1} \\ \ddot{y}_{r2} \end{bmatrix} \tag{4.31}$$

The trajectory pre-filter offsets the commanded trajectory independently for each end of the gantry to remove correlations of the commanded velocity, acceleration, jerk, and snap (4th derivative) profiles from the individual actuator servo errors:

$$\begin{aligned} y_{r1} &= y_r + K_{vel,1}\dot{y}_{rf} + K_{acc,1}\ddot{y}_{rf} + K_{jerk,1}\dddot{y}_{rf} + K_{snap,1}y_{rf}^{(IV)} \\ y_{r2} &= y_r + K_{vel,2}\dot{y}_{rf} + K_{acc,2}\ddot{y}_{rf} + K_{jerk,2}\dddot{y}_{rf} + K_{snap,2}y_{rf}^{(IV)} \end{aligned} \tag{4.32}$$

The mass distribution terms α_1 and α_2, the trajectory pre-filters and the feedforward inertia compensation have been gain-scheduled in terms of the x-axis position to account for inertia variations due to table motion,

49

$$\mathbf{M} = \mathbf{M}(x_r), \quad \alpha_1 = \alpha_1(x_r), \quad \alpha_2 = \alpha_2(x_r) \tag{4.33}$$

All filters were discretized using pole-zero matching with a sampling frequency of 15 kHz. When the design was complete, the peak sensitivity of 2.6 occurs at 40 Hz. The first crossover frequency was at 52 Hz. The controller was also active in the range of 83-124 Hz, corresponding to damping of the yaw mode. The MIMO loop magnitude and Nyquist plots are shown in Figure 4.13 and the sensitivity function is shown in Figure 4.14.
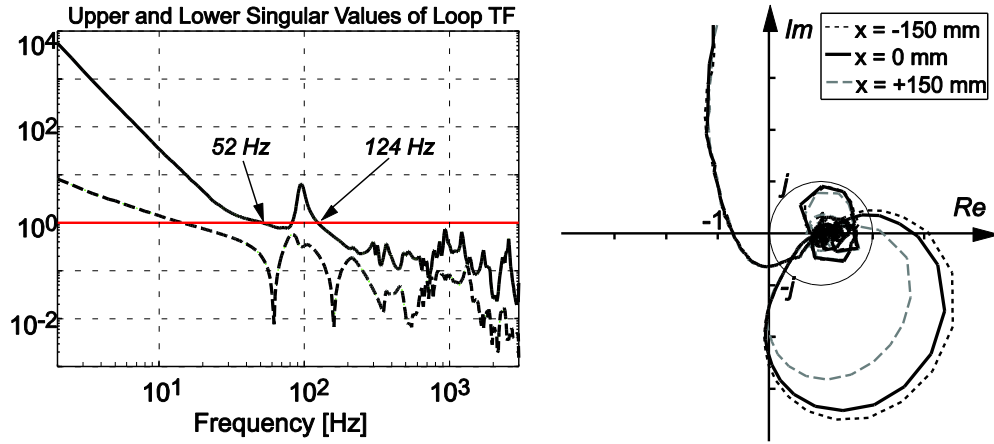

Figure 4.13: Y-axis loop transfer function upper and lower singular values (left) and MIMO Nyquist plot (right).
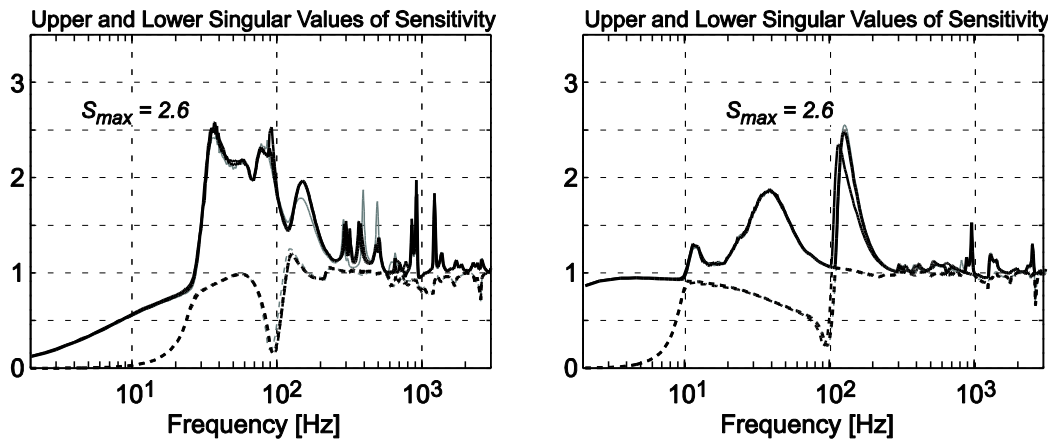

Figure 4.14: Upper and lower singular values of the sensitivity function for the proposed MIMO controller (left) and the SISO PID controllers (right).

50

When a decoupled PID controller with identical notch and low-pass filters was tuned to give a similar sensitivity peak (shown in Figure 4.14), the maximum achievable crossover frequency was only 16 Hz. Comparing the open- and closed-loop disturbances responses in Figure 4.15, when applying the MIMO control law the low frequency disturbance rejection is improved up to 28 Hz, and in a wide frequency band around the yaw mode (65-115 Hz). The yaw mode resonance is attenuated by a factor of ~5, with the vibration frequency shifting from 94 Hz to 105 Hz. On the other hand, the SISO PID controllers only provide improved disturbance rejection up to 10 Hz, and 2 times attenuation of the yaw mode resonance, while shifting it to 112 Hz, as seen in Figure 4.15.
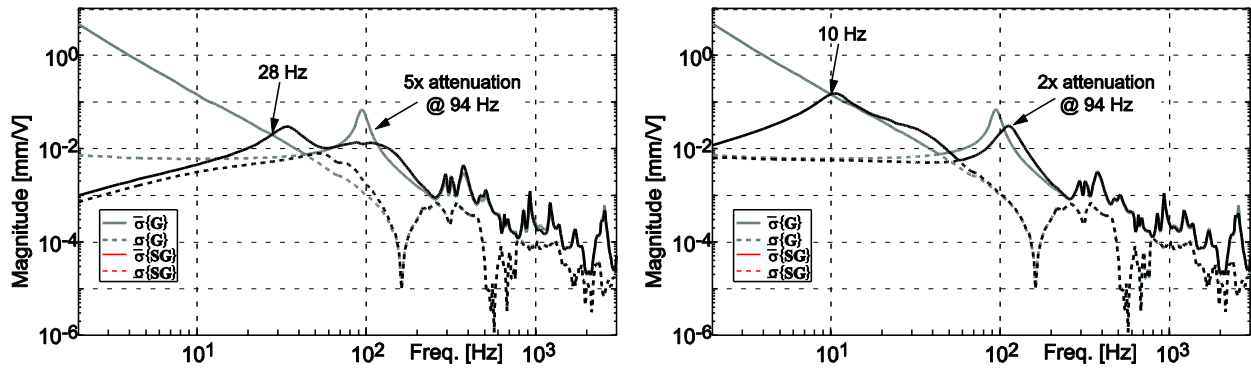

Figure 4.15: Singular values of open (G) and closed-loop (SG) transfer functions for the proposed MIMO controller (left) and independent SISO PID controllers (right).

4.5 Experimental Results

The developed control law has been compared to the standard approach of using independent PID controllers in step disturbance (i.e., rope-snap), tracking and contouring tests.

The improved disturbance rejection capability of the MIMO control law over the SISO controller can be seen in rope-snap tests, as shown in Figure 4.16. The tests consisted of applying a horizontal load of 57 N at the center of the worktable using a string and pulley system, and then cutting the string and monitoring the table motion. The table displacement was measured directly using a Renishaw RLE10 laser interferometer.
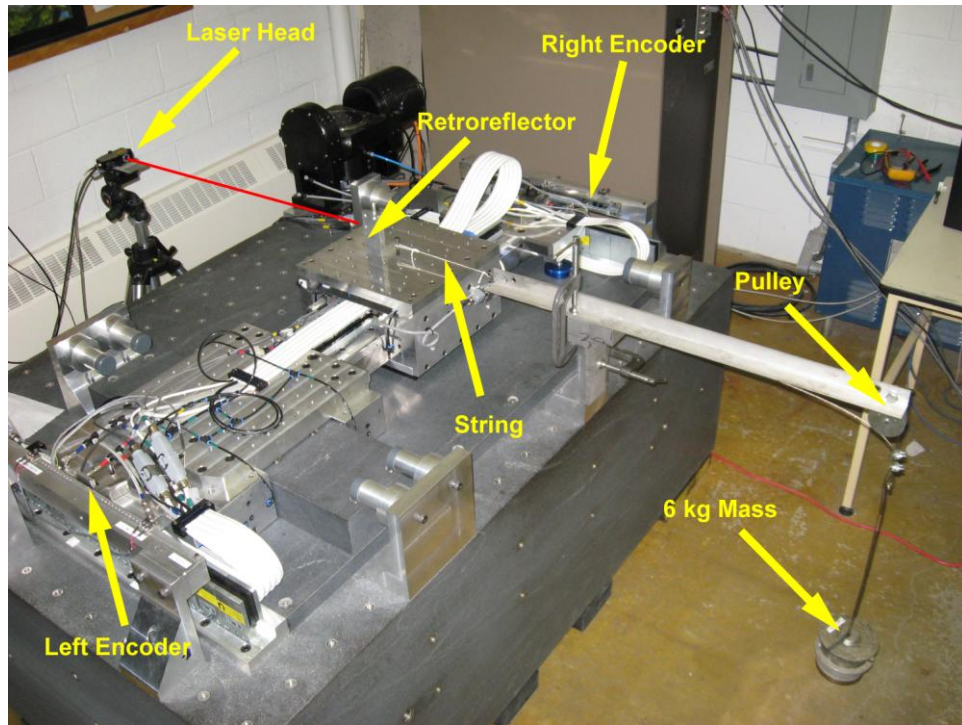
Figure 4.16: Experimental setup for step disturbance (i.e., rope-snap) testing

With the MIMO controller, the table motion had a significantly lower peak displacement of 6.6 um, compared to 30.3 um with the SISO controller. The initial displacement of 1.7 um measured by the laser interferometer is a result of the mechanical flexibility of the machine (approximately 32.5 N/um). The amplitude spectral density [22] shows significant disturbance rejection improvement at low frequencies. The 23 Hz vibrations seen in the MIMO response correspond to the machine base vibrations. The controller can be detuned to reduce these vibrations, or new machine supports can be designed to mitigate this problem further. Overall, the disturbance rejection improvement provided by the proposed MIMO controller over the mainstream method of applying independent PID's is very clear.
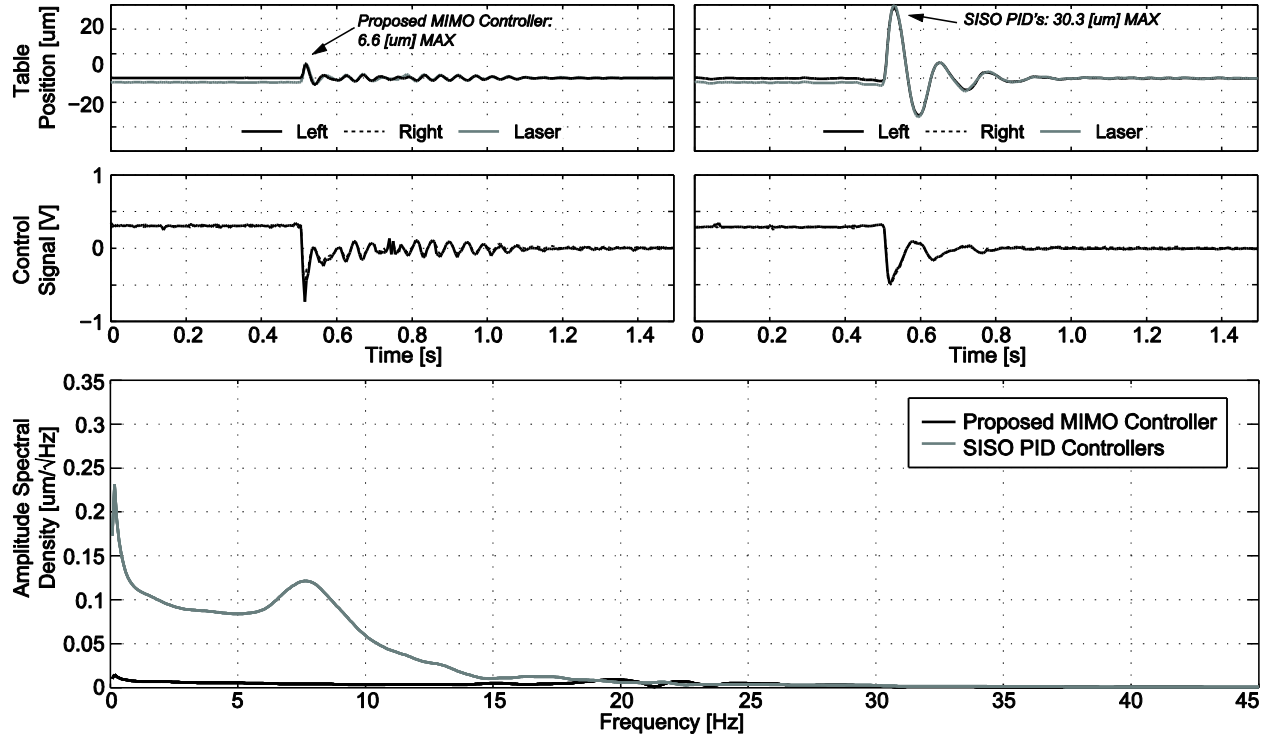
Figure 4.17: Table y-axis displacement, control signal and amplitude spectral density for MIMO (proposed) and SISO PID controllers during rope-snap tests.

The MIMO controller and SISO PID's have also been compared in tracking experiments, with the results shown in Figure 4.18. While tracking a jerk-continuous trajectory with 1 mm/s feed rate (2.8 mm/s^2 acceleration, 10 mm/s^3 jerk), the MIMO controller had 103 nm maximum (28 nm RMS) tracking error, compared to 331 nm maximum (87 nm RMS) for the SISO PID's. In high speed tracking tests (200 mm/s, 2 m/s^2 acceleration, 50 m/s^3 jerk), the MIMO controller held 1.68 um maximum and 0.28 um RMS accuracy. In the same test, the SISO PID controllers had 27.2 um maximum, 7.58 um RMS error. During 200 mm/s constant velocity motion, the MIMO controller held 0.37 um accuracy, compared to 2.4 um for the SISO PID's.

53
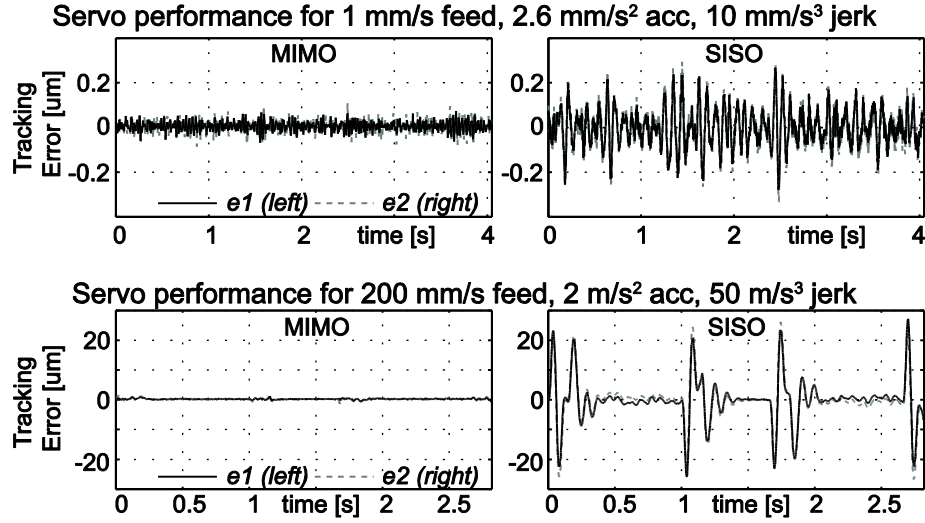
Figure 4.18: Y-Axis tracking performance for 1 mm/s and 200 mm/s for the proposed MIMO and SISO PID controllers.

The x-axis and y-axis controllers have similar tracking errors, as seen in Figure 4.19. During 1 mm/s tracking tests, the maximum and RMS errors were 106 nm and 25 nm, respectively. At 200 mm/s, they were 1.66 um and 0.296 um. The controller held 0.35 um accuracy during constant 200 mm/s velocity motion.
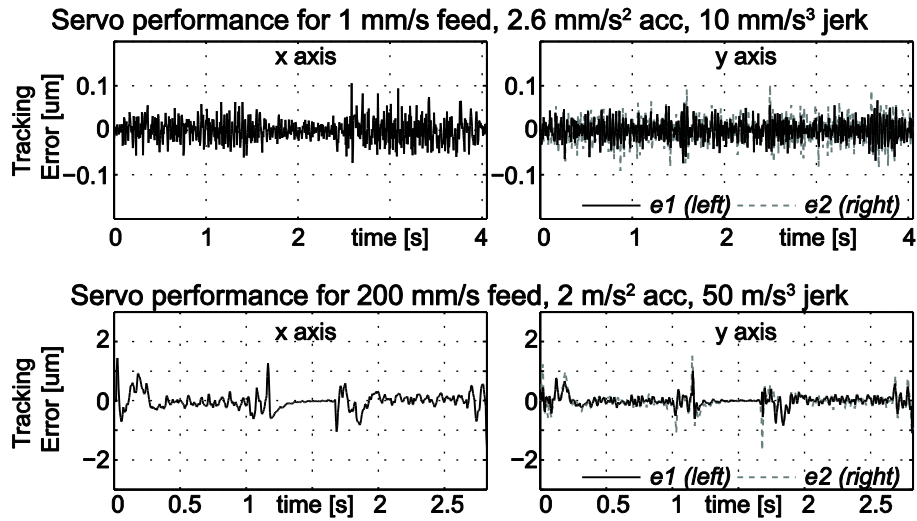
Figure 4.19: X and Y-axis tracking performance for the proposed controller.

The controller was also used to track circular and diamond contours. The machine can accurately track small feature sizes at low speeds, as shown in Figure 4.20. The circle has a diameter of 1.0 um, while the

54

diamond has a side length of 1.0 um. The contour errors are less than 85 nm, with RMS errors less than 25 nm, while contouring at 1 um/s.
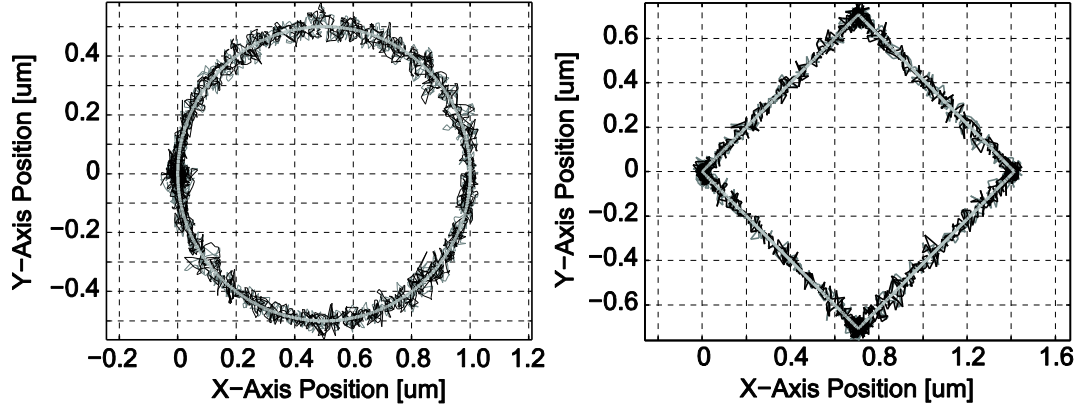
Figure 4.20: Contouring results for 1.0 um feature sizes at 1 um/s feedrate, 2.6 um/s^2 acceleration and 10 um/s^3 jerk.

When the feature size and speed are increased to 1 mm and 1 mm/s, as seen in Figure 4.21, the errors do not increase much. The maximum contouring errors are less than 130 nm, with RMS errors less than 30 nm. It is believed that the low speed tracking and positioning accuracy is greatly affected by the amplifier PWM and the use of analog signals for the control and encoder signals. Further research is being conducted into these sources of error, and efforts are underway to mitigate them (e.g., using linear amplifiers, better encoders and applying dynamic error budgeting).
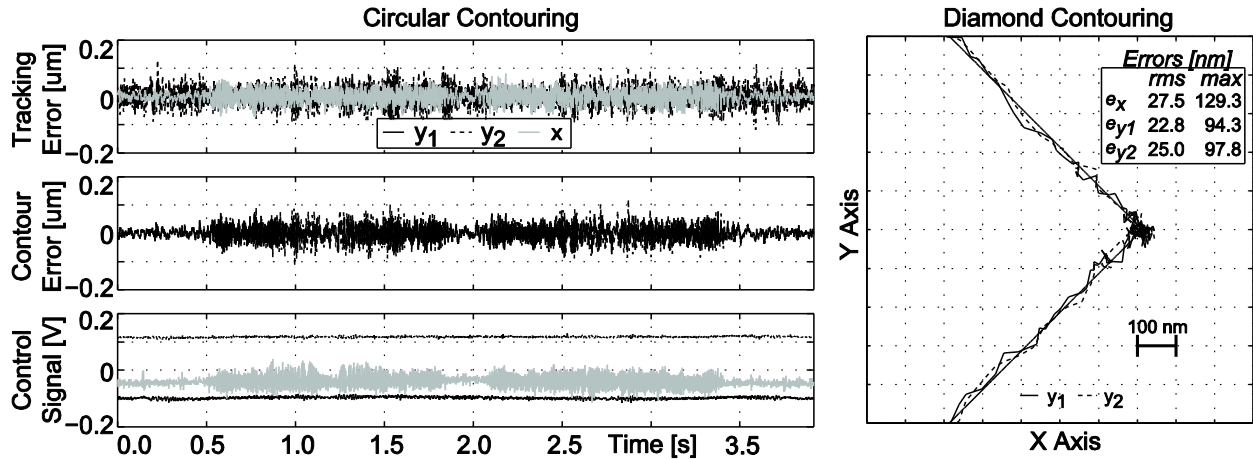
Figure 4.21: Contouring results for 1.0 mm feature sizes with 1 mm/s feedrate, 2.6 mm/s^2 acceleration and 10 mm/s^3 jerk.

55

Contouring results for 200 mm features at 200 mm/s are shown in Figure 4.22. The maximum contouring error for the circular trajectory is less than 1.9 um (RMS: 0.17 um), while for the diamond it is 2.23 um (RMS: 0.36 um).
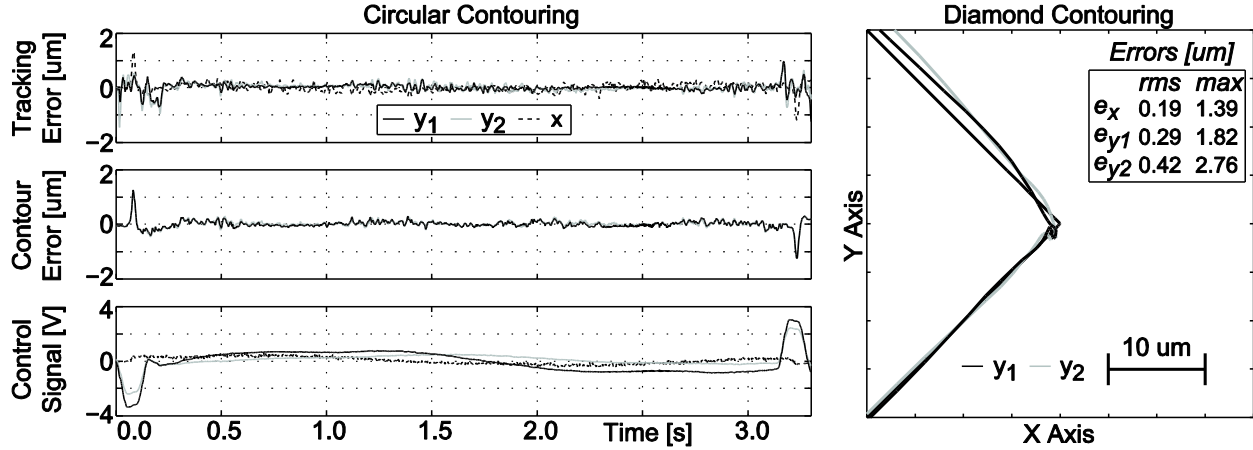
Figure 4.22: Contouring results for 200 mm feature sizes with 200 mm/s feedrate, 2 m/s^2 acceleration, 50 m/s^3 jerk.

4.6 Conclusions

This chapter has presented a new controller design for a T-type gantry stage driven by linear motors. The x-axis, which exhibits reasonably decoupled dynamics from the y-axis, was stabilized using loop shaping. This approach provides more versatility compared to the mainstream PID or P-PI cascade techniques. The y-axis design presented a more significant challenge, due to the dynamic coupling between the two actuation points through yaw vibrations, and also the variation of mass distribution as a function of x-axis position. A dynamic model was developed and identified, which captured both the yaw behavior and the influence of the x-axis position on the gantry's inertial properties. A control scheme was developed which achieves CoM position control through sensor/actuator averaging and loop shaping. Further stiffness and damping enhancements were realized through active vibration damping and actuator level integral action, both of which contributed to increased dynamic stiffness in coping with disturbance forces that can come from a cutting process. Adequate feedforward filters were developed to enhance the command following properties. One critical issue was guaranteeing adequate stability margins for the y-axis, which was achieved using multivariable frequency domain analyses. Effectiveness of the proposed control scheme has been validated in low (1 um/s) and high (200 mm/s) speed contouring tests, where servo accuracies between 85 nm and 1.9 um could be retained for circular and diamond interpolation trajectories.

56

Chapter 5
Conclusions

5.1 Conclusions

This thesis has presented new control techniques to improve dynamic accuracy and stiffness in ball screw drives and direct feed drives. The contributions of this thesis are summarized as follows:

A pole-placement based controller which provides motion control, disturbance rejection and active vibration damping for ball screw drives has been developed. This controller is based on a lumped parameter model of the drive which captures the dynamics of the first axial mode of the ball screw. Using insights from low authority control, physically motivated closed-loop pole locations can be chosen. Compared to other mode-compensating control laws in literature, the MC-PPC is simple to tune and provides comparable results. A bandwidth of 100 Hz has been realized, resulting in a servo accuracy of 3.9 um for a 1000 mm/s velocity with 1 g acceleration. The controller yielded a 40-55 percent improvement in peak error when compared to P-PI cascade control in tracking and machining tests.

In addition, a novel trajectory pre-filter has been designed, which is also easy to tune based on the results of a single tracking experiment. The effectiveness of the pre-filter has been shown in both ball screw drives and linear motor drives.

A new control law for a T-type gantry was developed, using sensor and actuator averaging and active vibration damping. Control of the CoM position was performed using a loop shaping filter, along with the sensor/actuator averaging scheme. Active vibration damping emulating a torsional damper was added to improve disturbance rejection and stability margins. When compared to the conventional approach of using independent SISO PID loops at the actuator level, the developed MIMO control law significantly improves the tracking performance and disturbance rejection of the stage. Contouring errors less than 100 nm were achieved for low speed circular and diamond trajectories. At 200 mm/s, dynamic accuracies of around 2 um were achieved.

5.2 Future Research

Further research on the ball screw drive could include using a more accurate dynamic model, which uses a full mass matrix. Such a model will capture the dynamics of the system more fully, and so may improve the controller performance. Also, more investigation into the contribution of the amplifier's current control loop should be conducted. In addition, work is currently being conducted into reducing the effects of lead error and other mechanical defects on the dynamic accuracy of the drive.

For the direct drive gantry stage, the coupling between the x- and y-axis should be quantified. During high speed contouring the assumption that the x-axis is independent of the gantry excitation is not valid. In addition, more detailed modeling of the linear motors which includes effects such as force ripples should be conducted. Also, further investigation of the shape of the vibration mode at 320 Hz is required. Construction of a Finite Element model of the gantry may give more insight into the higher order dynamics that have been observed. As mentioned previously, applying dynamic error budgeting to the stage may help to identify factors limiting the achievable tracking accuracies at low speeds. In particular, replacing the current PWM amplifier with a linear amplifier may help to improve low speed accuracy.

Currently, the main limitation preventing more aggressive control in the y-axis is the presence of machine base vibrations. Any improvements in the design of the machine supports would immediately yield dividends in terms of controller performance.

References

[1] Allotta, B., Angioli, F., Rinchi, M., 2001, Constraints Identification for Vibration Control of Time-Varying Boundary Conditions Systems, Proceedings of the 2001 IEEE/ASME International Conference on Advanced Intelligent Mechatronics (AIM), Vol. 1, pp. 606-611.

[2] Altintas, Y., Okwudire, C. E., 2009, Dynamic Stiffness Enhancement of Direct-Driven Machine Tools using Sliding Mode Control with Disturbance Recovery, Annals of the CIRP, 58/1:335-338.

[3] Altintas, Y., 2000, Manufacturing automation: metal cutting mechanics, machine tool vibrations, and CNC design, Cambridge University Press.

[4] Armstrong, H. B., Dupont, P., Canudas, D. W. C., 1994, A Survey of Models, Analysis Tools and Compensation Methods for the Control of Machines with Friction, Automatica, 30/7:1083-1138.

[5] Boerlage, M., Steinbuch, M., Tousain, R., 2004, Reference Trajectory Relevant Jerk Derivative Feedforward Control for Motion Systems, Proceedings of ASPE Control of Precision Systems, Cambridge, MA.

[6] Chen, Y., Tlusty, J., 1995, Effect of Low-Friction Guideways and Lead-Screw Flexibility on Dynamics of High-Speed Machines, Annals of the CIRP, 44/1:353-356.

[7] Cuttino, J. F., Dow, T. A., Knight, B. F., 1997, Analytical and Experimental Identification of Nonlinearities in a Single-Nut, Preloaded Ball Screw, Journal of Mechanical Design, Vol. 119, 15-19.

[8] Erkorkmaz, K., Kamalzadeh, A., 2006, High Bandwidth Control of Ball Screw Drives, Annals of the CIRP, 55/1:393-398.

[9] Erkorkmaz, K., Altintas, Y., 2001, High Speed CNC System Design. Part II: Modeling and Identification of Feed Drives, International Journal of Machine Tools and Manufacture, 41/10:1487-1509.

[10] Erkorkmaz, K., Altintas, Y., 2001, High Speed CNC System Design. Part III: High Speed Tracking and Contouring Control of Feed Drives, International Journal of Machine Tools and Manufacture, 41/11:1637-1658.

[11] Franklin, G.F., Powell, J.D., Emami-Naeini, A., 2005, Feedback Control of Dynamic Systems (5th Edition), Prentice Hall.

[12] Gawronski, W.K., 1998, Dynamics and control of structures: A modal approach, Springer NY.

[13] Giam, T. S., Tan, K. K., Huang, S., 2007, Precision Coordinated Control of Multi-Axis Gantry Stages, ISA Transactions, 46/3:399-409.

[14] Gordon, D., Erkorkmaz, K., 2010, Precision Control of a Linear Motor Driven Gantry using Sensor/Actuator Averaging and Active Vibration Damping, Proc. of 2nd CIRP-PMI, Vancouver.

[15] Gordon, D. J., Erkorkmaz, K., 2009, Accurate Control of Ball Screw Drives using Pole-Placement Based Vibration Damping and Optimized Trajectory Pre-Filtering, Proceedings of the 24th ASPE Annual Meeting, Monterey, CA, 211-214.

[16] Hyde, J. M., Seering, W. P., 1991, Using Input Command Pre-Shaping to Suppress Multiple Mode Vibration, Proceedings of the IEEE International Conference on Robotics and Automation, Vol. 3, 2604-2609.

[17] Jones, S. D., Ulsoy, A. G., 1999, An Approach to Control Input Shaping with Application to Coordinate Measuring Machines, Journal of Dynamic Systems, Measurement, and Control, 21/2:242-247.

[18] Kalman, R. E., 1960, A New Approach to Linear Filtering and Prediction Problems, Journal of Basic Engineering, Vol. 82, 35-44.

[19] Kamalzadeh, A., Erkorkmaz, K., 2007, Compensation of Axial Vibrations in Ball Screw Drives, Annals of the CIRP, 56/1:373-378.

[20] Kautsky, J., Nichols, N. K., Van Dooren, P., 1985, Robust Pole Assignment in Linear State Feedback, International Journal of Control, 41/5:1129-1155.

[21] Lee, H. S., Tomizuka, M., 1996, Robust Motion Controller Design for High-Accuracy Positioning Systems, IEEE Transactions on Industrial Electronics, 43/1:48-55.

[22] Monkhorst, W., 2004, M.Sc. Thesis: Dynamic Error Budgeting, A Design Approach. Delft University of Technology, Delft.

[23] Ogata, K., 2002, Modern control engineering, Prentice Hall.

[24] Ogata, K., 1995, Discrete-time control systems, Prentice-Hall, Inc. Upper Saddle River, NJ, USA.

[25] Okwudire, C., Altintas, Y., 2009, Minimum Tracking Error Control of Flexible Ball Screw Drives using a Discrete-Time Sliding Mode Controller, Journal of Dynamic Systems, Measurement, and Control, 131, 051006.

[26] Okwudire, C., 2005, M.Sc. Thesis: Finite Element Modeling of Ballscrew Feed Drive Systems for Control Purpose. University of British Columbia, Vancouver, Canada.

[27] Okwudire, C. E., 2009, Ph.D. Thesis: Modeling and Control of High Speed Machine Tool Feed Drives. University of British Columbia, Vancouver, Canada.

[28] Pritschow, G., 1998, A Comparison of Linear and Conventional Electromechanical Drives, Annals of the CIRP, 47/2:541-548.

[29] Pritschow, G., 1996, On the Influence of the Velocity Gain Factor on the Path Deviation, Annals of the CIRP, 45/1:367-371.

[30] Pritschow, G., Philipp, W., 1992, Research on the Efficiency of Feedforward Controllers in Direct Drives, Annals of the CIRP, 41/1:411-415.

[31] Schäfers, E., 2006, Mechatronic Modeling and Analysis of Machine Tools, Proc. 2nd Internation Conference on High Performance Cutting (CIRP-HPC'06), Vancouver.

[32] Skogestad, S., Postlethwaite, I., 2005, Multivariable Feedback Control: Analysis and Design (2nd Edition), Wiley.

[33] Smith, A. D., 1999, Ph.D. Thesis: Wide Bandwidth Control of High-Speed Milling Machine Feed Drives. University of Florida, Department of Mechanical Engineering, Florida.

[34] Symens, W., Van Brussel, H., Swevers, J., 2004, Gain-Scheduling Control of Machine Tools with Varying Structural Flexibility, Annals of the CIRP, 53/1:321-324.

[35] Teo, C. S., Tan, K. K., Lim, S. Y., Huang, S., Tay, E. B., 2007, Dynamic Modeling and Adaptive Control of a H-Type Gantry Stage, Mechatronics, 17/7:361-367.

[36] Tomizuka, M., 1987, Zero Phase Error Tracking Algorithm for Digital Control, ASME Journal of Dynamic Systems, Measurement, and Control, Vol. 109, 65-68.

[37] Van Brussel, H., Van Den Braembussche, P., 1998, Robust Control of Feed Drives with Linear Motors, Annals of the CIRP, 47/1:325-328.

[38] Varanasi, K. K., Nayfeh, S. A., 2004, The Dynamics of Lead-Screw Drives: Low-Order Modeling and Experiments, Journal of Dynamic Systems, Measurement, and Control, Vol. 126, 388-396.

[39] Weck, M., Ye, G., 1990, Sharp Corner Tracking using the IKF Control Strategy, Annals of the CIRP, 39/1:437-441.

[40] Weng, M. -., Lu, X., Trumper, D. L., 2002, Vibration Control of Flexible Beams using Sensor Averaging and Actuator Averaging Methods, IEEE Transactions on Control Systems Technology, 10/4:568-577.

[41] Won, M., Hedrick, J. K., 2001, Disturbance Adaptive Discrete-Time Sliding Control with Application to Engine Speed Control, ASME Journal of Dynamic Systems, Measurement and Control, Vol. 123, 1-9.

[42] Zaeh, M. F., Oertli, T., Milberg, J., 2004, Finite Element Modeling of Ball Screw Feed Drive Systems, Annals of the CIRP, 53/1:289-292.

[43] Zatarain, M., Ruiz de Argandoña, I., Illarramendi, A., Azpeitia, J. L., Bueno, R., 2005, New Control Techniques Based on State Space Observers for Improving the Precision and Dynamic Behaviour of Machine Tools, Annals of the CIRP, 54/1:393-396.